Article

Spatial heterogeneity accelerates phase-to-trigger wave transitions in frog egg extracts

Owen Puls[1,2,6], Daniel Ruiz-Reynés [3,4,6], Franco Tavella [2,5], Minjun Jin[2,5], Yeonghoon Kim [2], Lendert Gelens [3,6] ✉ & Qiong Yang [1,2,5,6] ✉

Cyclin-dependent kinase 1 (Cdk1) activity rises and falls throughout the cell cycle: a cell-autonomous process called mitotic oscillations. Mitotic oscillators can synchronize when spatially coupled, facilitating rapid, synchronous divisions in large early embryos of *Drosophila* (~0.5 mm) and *Xenopus* (~1.2 mm). Diffusion alone cannot achieve such long-range coordination. Instead, studies proposed mitotic waves—phase and trigger waves—as mechanisms of the coordination. How waves establish over time remains unclear. Using *Xenopus laevis* egg extracts and a Cdk1 Förster resonance energy transfer sensor, we observe a transition from phase to trigger wave dynamics in initially homogeneous cytosol. Spatial heterogeneity promotes this transition. Adding nuclei accelerates entrainment. The system transitions almost immediately when driven by metaphase-arrested extracts. Numerical simulations suggest phase waves appear transiently as trigger waves take time to entrain the system. Therefore, we show that both waves belong to a single biological process capable of coordinating the cell cycle over long distances.

Cell division, one of the most important processes in biology, is regulated by a well-studied pacemaker oscillator centered on the cyclin B-Cdk1 complex, known as the mitotic clock[1,2] (Fig. 1a). The mitotic cell cycle, specifically the DNA-replication-and-division cycle, undergoes a sequence of events in which cells replicate DNA and partition the copies into daughter cells such that each daughter receives precisely one copy of the genome[3].

In the early embryogenesis of organisms such as *Xenopus* or *Drosophila*, cells initially proceed through a series of fast divisions[4,5]. These mitotic cycles lack many features of mature cells—e.g., gap phases, cell cycle checkpoints, and zygotic gene transcription—which only arise after the mid-blastula transition (MBT)[6]. For this reason, it is key for these cycles to remain roughly synchronized prior to MBT, even though some desynchronization is tolerated[7]. Throughout this process, mitotic events occur within minutes of each other. However, due to the large cell size in such embryos, diffusion alone remains far too slow to synchronize the system: such a process would take multiple hours, not minutes[8–12].

Previous studies have identified waves of mitotic events, both in vitro[8] and in vivo[9], which propagate at speeds sufficiently high to communicate across the lengths of the embryo. Trigger waves (~40–60 μm/min), resulting from the coupling of diffusion and local dynamics[10,11], were first shown to coordinate mitosis in *Xenopus* extracts, using nuclear envelope breakdown (NEB) to illustrate their propagation after a few early, largely synchronous cycles[8]. Subsequent work revealed that the nucleus itself serves as the pacemaker for these waves, locally accelerating oscillations possibly by aggregating cell cycle regulators and thus driving waves[13,14]. This aggregating mechanism was later confirmed in individual oscillating microemulsions[15]. In vivo, it is known time-dependent Cdk1 gradients guide surface contraction waves (SCWs) in starfish oocytes[16,17], and there is evidence Cdk1 trigger waves are responsible for these SCWs in

[1]Department of Physics, University of Michigan, Ann Arbor, MI 48109, USA. [2]Department of Biophysics, University of Michigan, Ann Arbor, MI 48109, USA. [3]Laboratory of Dynamics in Biological Systems, KU Leuven, Department of Cellular and Molecular Medicine, University of Leuven, B-3000 Leuven, Belgium. [4]IFISC (CSIC-UIB). Instituto de Física Interdisciplinar y Sistemas Complejos, E-07122 Palma de Mallorca, Spain. [5]Department of Computational Medicine and Bioinformatics, University of Michigan, Ann Arbor, MI 48109, USA. [6]These authors contributed equally: Owen Puls, Daniel Ruiz-Reynés, Lendert Gelens, Qiong Yang. ✉e-mail: lendert.gelens@kuleuven.be; qiongy@umich.edu
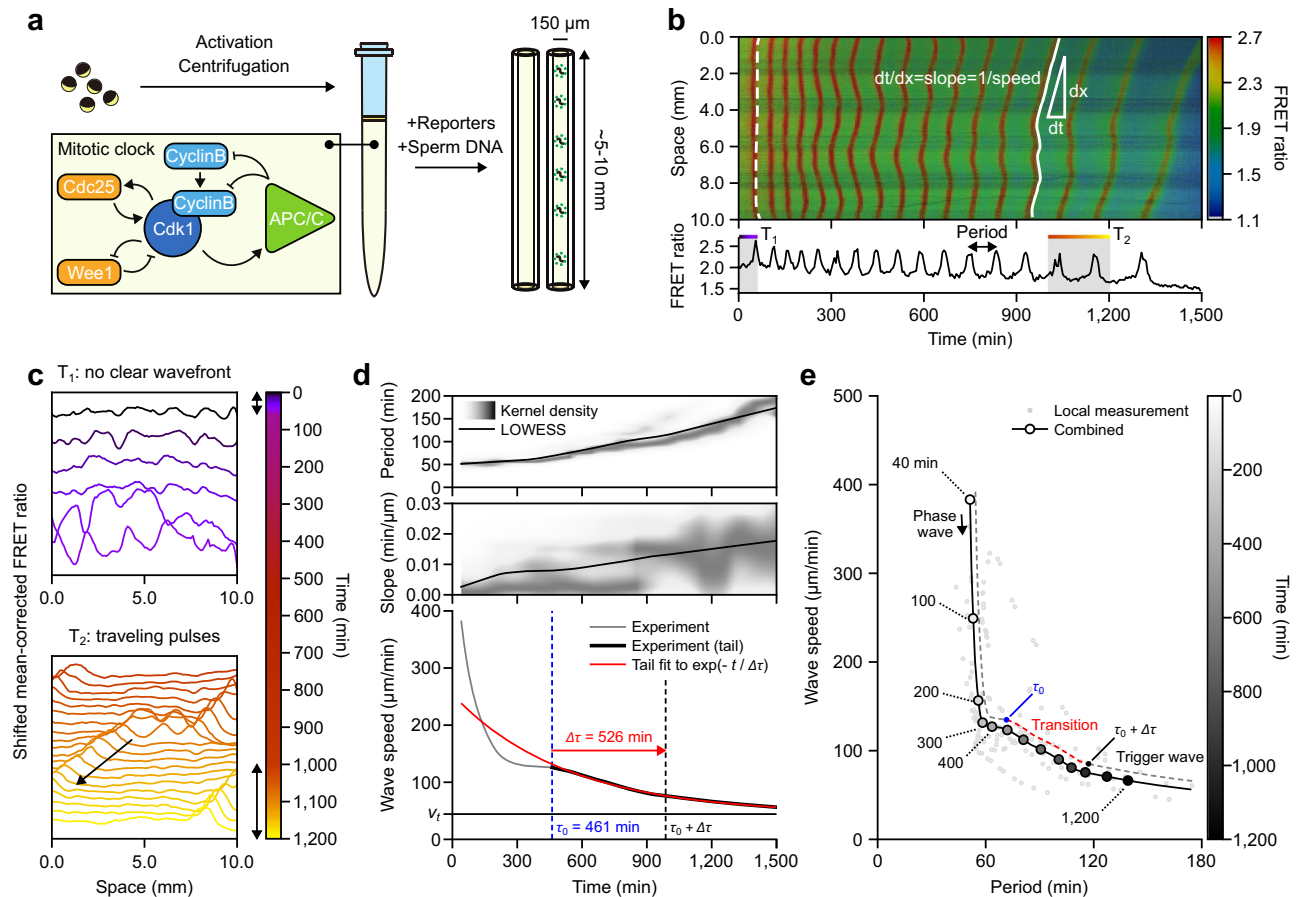
Fig. 1 | Time evolution of mitotic waves. a Schematic view of the experimental preparation of cycling egg extracts in Teflon tubes. Bottom-Left: The regulatory network driving mitotic oscillations. **b** Top: Representative FRET ratio kymograph for extracts without sperm DNA. Color bar indicates FRET ratio. Two wavefronts are labeled in white (dashed, early time; solid, later time). The local wave speed is the inverse of the wavefront slope (dt/dx). Bottom: FRET ratio time course recorded at $x = 10$ mm. The period is defined as the interval between consecutive FRET ratio peaks. One early time region, T_1, and one later time region, T_2, are selected for (**c**). **c** Shifted mean-corrected FRET ratio for T_1 and T_2. Top: T_1 showing in-phase activation with no clear wavefront. Bottom: T_2 showing a traveling pulse, indicated by an arrow. Bidirectional arrows beside the colorbar indicate T_1 and T_2. **d** Time evolution of the period (top), slope (middle), and wave speed (bottom). Period and slope distributions (grayscale colormap) represent the time-normalized kernel density estimation. The solid curves show the locally weighted scatterplot smoothing (LOWESS) estimations. The speed here is the inverse of the slope's LOWESS estimation. The onset of exponential decay (τ_0, dashed blue line) is calculated via a moving horizon fitting (see Supplementary Fig. 1). The speed after τ_0 is fitted by an exponential function (solid red line) to calculate the entrainment time ($\Delta\tau$). The horizontal black line indicates the fitted terminal speed (v_t) and the vertical dashed black line indicates $\tau_0 + \Delta\tau$. **e** Speed-period relationship. Local measurements of the period and speed are represented by gray dots (2 % of all data points were shown). Combined speed-period relation (solid black line) is computed from the LOWESS estimations in (**d**). Markers (open circles with grayscale fillings) indicate multiples of 100 min (except for the first, shown for clarity). Color bar indicates time. The transition time points τ_0 and $\tau_0 + \Delta\tau$ are indicated on a dashed guideline with the transition window highlighted in red. Data in (**d**, **e**) are pooled from two independent egg batches with three replicates each ($n = 6$).

the first cell cycle of the *Xenopus laevis* frog embryo[8]. However, it remains unclear whether SCWs in the subsequent cell cleavages in the frog embryo are also controlled by Cdk1 trigger waves. Moreover, the classical trigger wave mechanism may not be the sole contributor to the fast wave propagation observed in the early embryos.

Like *Xenopus* and other metazoans, the fruit fly embryo undergoes a series of rapid, roughly synchronous (and in this case, syncytial) divisions post-fertilization[6]. However, *Drosophila* embryos display waves of mitotic completion that traverse the entirety of the embryo (hundreds of microns) in mere minutes at early stages, with speeds much faster (~100 μm/min) than what would be considered achievable by traditional trigger wave models[9]. Moreover, these embryos exhibit distinct spatial dynamics that forgo the classical picture of a stable regime invading into and promoting a metastable regime[10,11]. Instead, spatial gradients in Cdk1 activity are largely preserved, while the overall levels are swept upwards[18].

Vergassola et al. propose that phase waves[12] are responsible for the ultra-fast waves observed in vivo[12,18] and describe how the spatial

gradients of Cdk1 activity first form and introduce delays across different positions that are preserved in time. Phase waves appear to spread due to local phase gradients but are not actively spread by mutual interactions, in contrast with trigger waves, which do propagate through a coupling of diffusion and local reactions[8–12]. The authors suggest that a time-dependent sweeping-up of Cdk1 activity leads to wave-like behavior spreading at scales faster than trigger waves, consistent with phase waves. Interestingly, these rapid phase waves observed in wild-type embryos transition to slower, classical bistable waves in mutant embryos lacking the mitotic switch feedback, suggesting a phase-to-trigger wave transition in *Drosophila* embryos[18]. This shift was linked to period lengthening in later cycles, due to increased activation of Chk1[18]. The authors provided further experimental evidence to demonstrate that slowing the cell-cycle progression through genetic perturbations can result in trigger rather than phase waves[19]. Moreover, they showed that introducing spatial heterogeneity in nuclear density also generates trigger waves[19], highlighting the role of nuclei as seen in *Xenopus* extracts. The authors

speculated a similar phase-to-trigger wave transition, either through period lengthening or spatial heterogeneity, could exist in *Xenopus* and called for direct measurements of Cdk1 activity to resolve this open question[19].

In this work, we present direct evidence of mitotic waves in *Xenopus* extracts using a Förster resonance energy transfer (FRET) sensor that measures the ratio of activity between Cdk1 and its opposing phosphatase. We show that waves of Cdk1 activity can form spontaneously in the absence of nuclear pacemakers, sharing the fundamental nature of the classical chemical waves in a Belousov-Zhabotinsky (BZ) reaction-diffusion system. We investigate the time-dependent behavior of mitotic waves in *Xenopus* extracts, revealing a period-lengthening-independent transition from phase-wave-like to trigger-wave-like patterns over time, and as a result, offer the connecting thread between these phenomena. We also probe the role of nuclei in wave propagation, showing that in addition to acting as pacemakers, nuclei accelerate the entrainment of the system to the trigger wave regime. Building on the findings in these experiments, we then propose an effective method for generating directed waves in vitro, which reinforces the notion of entrainment explicitly. In short, we use a reservoir of active Cdk1 to drive waves through the oscillating medium. Taken together, we offer a general picture of the interplay between phase and trigger waves and the role of heterogeneities in the spatial coordination of mitosis in the *Xenopus laevis* cytoplasm.

Results

Mitotic waves transition from phase waves to trigger waves

We leverage in vitro cell-free *Xenopus laevis* egg extracts to characterize mitotic waves. A schematic view of the experimental setup is presented in Fig. 1a. Cycling extracts are prepared following the protocol described in previous studies[20,21]. Instead of relying on downstream events such as NEB, we employ a FRET sensor to report the Cdk1 kinase activity, which allows us to directly visualize mitotic waves over time in *Xenopus*[15]. Cycling extracts supplemented with the Cdk1 FRET sensor are then loaded into ~5–10 mm long Teflon-coated tubes, submerged under mineral oil, and imaged using time-lapse epifluorescence microscopy.

In a representative experiment (Fig. 1b; Supplementary Movie 1), the FRET signal is represented by a heatmap with cool colors corresponding to low Cdk1 activity, and warm colors to high activity. High-activity regions can be clustered together via peak detection, allowing us to individualize wavefronts. Two wavefronts at different time regions are highlighted for comparison (Fig. 1b, top, white lines). Qualitatively, one can observe a difference between early time patterns that are largely synchronous and fast moving (Fig. 1b, top, dashed white line), and later time patterns which form linear fronts (Fig. 1b, top, solid white line). The explicit time evolution of the FRET signal is also depicted for a small slice (at position $x = 10$ mm; Fig. 1b, bottom). When plotting the FRET ratio spatial profile over consecutive frames for early and late cycles (Fig. 1c), we observe clear changes in spatial profiles over time. Early patterns (T_1: 0–60 min) resemble phase waves: a roughly uniform upswing in activity, and preservation of local peaks and spatial gradients (Fig. 1c, top), sharing similar features as those reported in Hayden et al.[19]. Conversely, at late times (T_2: 1000–1200 min), the system exhibits clearly linear, trigger-wave-like fronts, characterized by traveling pulses (Fig. 1c, bottom). This implies a transition from phase waves at early, fast cycles, to trigger waves at late, slower cycles.

To quantify this transition, we choose to measure the period and wave speed. The period is calculated as the peak-to-peak time between wavefronts (Fig. 1b, bottom; Fig.1d, top). Since the speed of early time patterns is often infinite at this resolution, we calculate the instantaneous derivative (slope, dt/dx) of the interpolated kymograph, using its reciprocal as an indicator of wave speed. In both cases, we estimate the kernel density of the data over time. We observe that the LOWESS

estimate for the period closely follows the peaks in density (Fig. 1d, top). However, this is not the case for the slope. The slope density shows low values at early times, high values at later times, and a mixture in between, suggesting a transition between different types of waves (Fig. 1d, middle). Wave speeds are obtained by inverting the LOWESS slope estimate, showing a monotonic decrease over time (Fig. 1d, bottom). The decrease in wave speed seems to follow a two-step process with an initial fast decay and a slower transition to a terminal speed (v_t). We quantify this transition following a moving horizon fitting algorithm (see Methods). Briefly, we find the potential transition starting time point (τ_0) that gives the best fit for exponential decay of the signal at late times (Supplementary Fig. 1). This time point tells us when waves start to relax exponentially towards the trigger wave state of later times. From the fitted exponential function, we extract a relaxation time scale ($\Delta\tau$) and thus fully quantify how long the system takes to transition between each state. For this data, wave speeds start to decay exponentially after $\tau_0 = 461$ min (Fig. 1d, bottom, dashed blue line) with a relaxation time scale of $\Delta\tau = 526$ min (Fig. 1d, bottom, red arrow). Interestingly, despite changes in period and wave speed, the FRET ratio maximum activation rate (dA/dt), calculated as the largest time derivative of the FRET ratio per cycle, remains relatively constant for the duration of the experiment (Supplementary Fig. 2).

When combined, our measurements reveal that the wave speed monotonically decreases as the cell cycle period lengthens (Fig. 1e). At early times (before τ_0), the period is short, and the system exhibits phase waves at diversified speeds of 400–100 μm/min, which are much faster than trigger waves. However, these transients eventually die off as the system transitions to a regime quasi-dominated by trigger waves (100–50 μm/min). This speed-period relation also appears to confirm a sweep-to-trigger transition, reported in fly embryos upon genetic perturbations[19], though in this case, we directly observed the transition as an inherent temporal evolution of the system, independent of external induction, thus bridging our understanding of mitotic waves between different model systems.

Transient dynamics explains phase-to-trigger wave transition

The observed transition from fast phase waves to slow trigger waves could be a result of two time-dependent factors. Firstly, we observed period lengthening, which suggests a potential time dependence in the intrinsic biochemical properties of the oscillator. This period lengthening is also commonly seen in cell-free extracts encapsulated in micro-scale droplets, whether or not nuclei are present, and can potentially be explained by ATP depletion[20,22] or the degradation of clock molecules such as cyclin B mRNA[23]. Notably, this elongation predominantly impacts the interphase, while the mitotic phase duration and Cdk1 activation profile remain largely unchanged[15,22]. Secondly, if we consider trigger waves as the attractor state of a dynamical system, the transition may imply a relaxation towards this state, a time-evolving process that necessitates a finite amount of time for a transient state (from a wide variety of initial conditions) to establish into a stable solution (attractor).

We turn to mathematical modeling to quantify the effect of these two hypothetical contributions to the wave dynamics we observed. We use a cell-cycle model introduced by Yang and Ferrell[24] and then later extended by Chang and Ferrell[8] to describe mitotic waves. The model describes the time evolution of active (denoted as a) and total cyclin B-Cdk1 (denoted as c) concentration (Eqs. (1) and (2), where $V(\mathbf{x}, t) = 0$ in the absence of nuclei). Cyclin B is synthesized at a rate k_s and then rapidly binds to Cdk1. The activity of the cyclin B-Cdk1 complex is regulated by phosphatase Cdc25, which activates the complex by dephosphorylation, and kinases Wee1 and Myt1, which deactivate the complex by phosphorylation. Finally, high Cdk1 activity leads to the activation of anaphase-promoting complex/cyclosome (APC/C), which targets cyclin B for degradation (Fig. 1a). The reaction rates are

described by ultrasensitive response curves dependent on the cyclin B-Cdk1 activity and parameterized based on experiments[24]. Diffusion is incorporated into the model to simulate spatially extended dynamics.

To replicate the observed period lengthening, we introduce an explicit time dependence to the mitotic regulatory network. Adopting a methodology similar to Rombouts and Gelens[25,26], we explore how the model parameters influence the period and activation rate (da/dt), which we use to compare to their experimentally observable counterparts (period and maximum activation rate dA/dt, extracted from the FRET signal time traces, respectively). We further modify the model equations with dimensionless factors α, β, η to examine the significance of the key network components (Fig. 2a). Factor α scales the activation and inactivation rates of Cdk1, which constitute the bistable switch at the mitotic network core. Numerical simulation shows that the period remains almost unaffected by α (Figs. 2a and S3, left). Factor β controls how fast cyclin B is synthesized and degraded, thus being fundamental for driving oscillations through the bistable trigger and negative feedback. Scaling β leads to a modulation of the

period (interphase lengthening) and mostly unchanged activation rate (Figs. 2a and S3, middle). Finally, factor η corresponds to a global time scaling, thus affecting every observable (Figs. 2a and S3, right). Out of the three modifications, changing β produces the most similar behavior to our experimental observations: the period lengthens without a significant change in activation rate. Therefore, by dialing the bistable trigger over time (decreasing β), we obtain a phenomenological model that reproduces the observed cell cycle behaviors.

To model relaxation dynamics, we incorporate a heterogeneous spatial profile of the cyclin synthesis rate $k_s(x)$. The loci with smaller periods in this profile (corresponding to larger values of $k_s(x)$) can act as trigger wave sources, as explored in previous works for pointlike sources[25,26]. Thus, we perform numerical simulations incorporating these two contributions: a time-dependent $\beta(t)$ (Fig. 2b, top) and a noisy $k_s(x)$ distributed across space (Fig. 2b, left). The diffusion rate is set to be 240 µm²/min, compatible with a rate reported in the fly embryo[9], to reproduce the wave speed at the end of the extract lifetime (≳1000
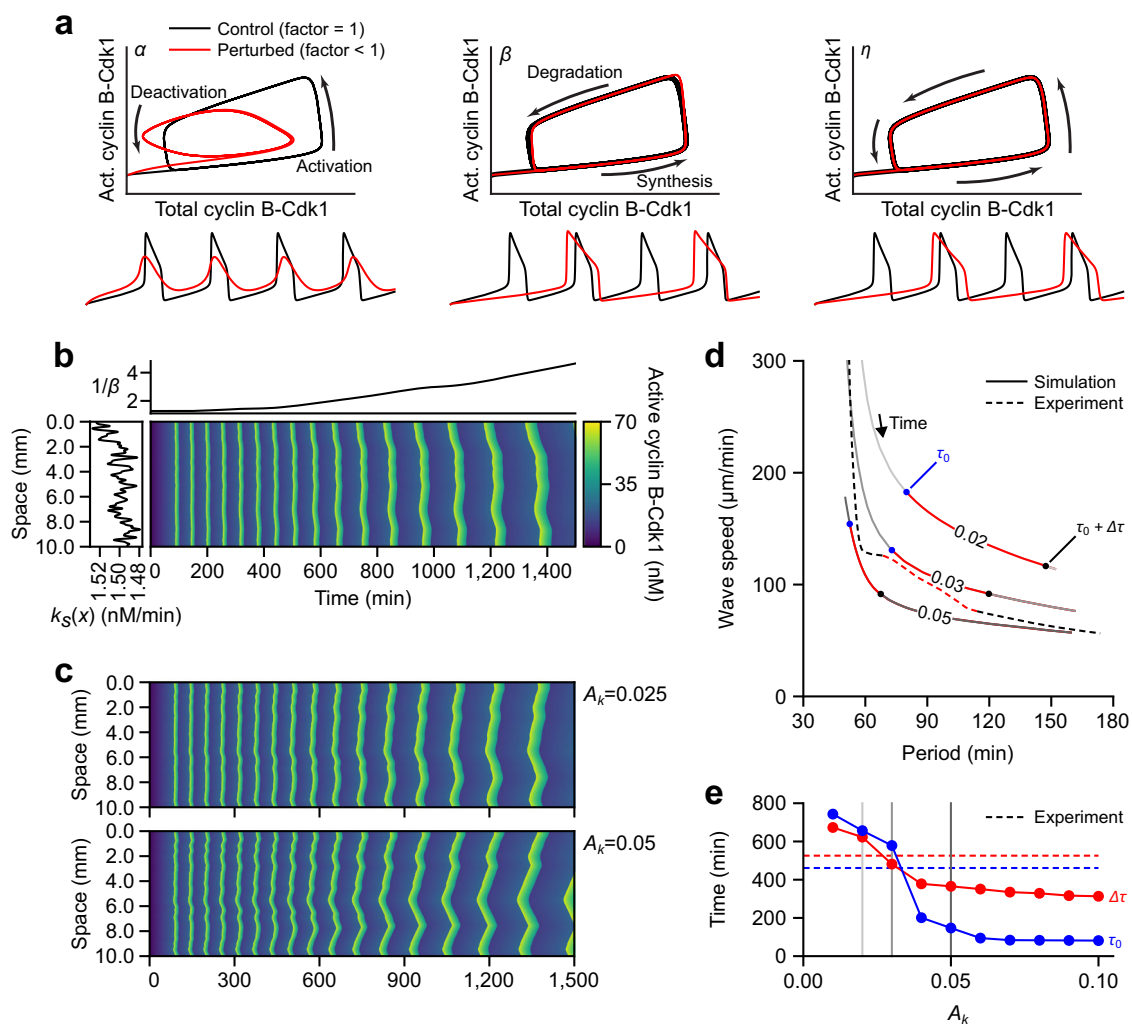
Fig. 2 | Mathematical modeling explains the transition from phase to trigger waves. a Schematic representation of the mitotic dynamics influenced by scaling factors α (left), β (middle), and η (right), which scale for the rates of respective reactions indicated by black arrows. See Methods and Supplementary Fig. 3 for details. Unperturbed (scaling factor = 1, black lines) and perturbed (scaling factor < 1, red lines) dynamics are compared for phase-plane trajectories of total and active cyclin B-Cdk1 concentration (top) and active cyclin B-Cdk1 concentration time courses (bottom). **b** Spatiotemporal evolution of the cyclin B-Cdk1 activity showing the transition from fast to slow waves. Simulation has incorporated the

experimental time-dependence of the period shown as $1/\beta(t)$ (top panel) and spatial variability in the synthesis term $k_s(x)$ (left panel, see also Methods). **c** Influence of spatial heterogeneity (A_k) on the wave speed entrainment. **d** Speed-period relation of the experiment (dashed line) and the numerical simulations (solid lines with respective A_k values labeled). The transition points τ_0 and $\tau_0 + \Delta\tau$ are marked as in Fig. 1e. The time frames between τ_0 and $\tau_0 + \Delta\tau$ are highlighted in red. **e** Dependence of transition time scales τ_0 (blue) and $\Delta\tau$ (red) on spatial heterogeneity. Experimental measurements are given in dashed lines. Vertical lines correspond to simulation conditions illustrated in (**d**) with matching grayscale colors.

min). The simulated kymograph in Fig. 2b captures both the period lengthening of waves and the gradual formation of slow linear fronts that resemble the qualitative observations from experiments. The formation of linear fronts is influenced by the noise level, denoted by A_k (see Methods for the definition); comparing two simulations with different levels of spatial noise, we find that large heterogeneity ($A_k = 0.05$) entrains the system more rapidly than small heterogeneity ($A_k = 0.025$), leading to a faster reduction to a wave speed that is characteristic of a trigger wave (Fig. 2c).

Applying the same analysis used for experimental data allows us to plot the speed-period relation for various heterogeneity levels (Fig. 2d). Keeping in mind that the period is a monotonically increasing function of time, we observe that the transition from phase waves to trigger waves happens both earlier (τ_0, blue dots) and faster ($\Delta\tau$, red regions, end with black dots) as the heterogeneity rises. $A_k = 0.03$ gives a result that quantitatively agrees with experiments, characterized by a two-step decay with $\tau_0 = 579$ min and $\Delta\tau = 482$ min.

Finally, we analyze the dependence of the transition time scales on the level of heterogeneity A_k (Fig. 2e). Increasing spatial heterogeneity significantly speeds up the transition to trigger waves, occurring both earlier (Fig. 2e, blue) and faster (Fig. 2e, red). Additionally, we find that suppressing the period elongation does not affect the speedup resulting from increased spatial heterogeneity (Supplementary Fig. 4). Therefore, the dominant effect in the transition from fast

phase waves to slow trigger waves is the finite relaxation time required by traveling waves to establish themselves, rather than the period lengthening itself. All in all, our modeling suggests that this transition can be sped up by introducing spatial heterogeneity into our system.

Nuclei speed up the transition from phase to trigger waves

The question then arises: how can we incorporate spatial heterogeneity in our experimental system? One possible approach is to introduce nuclei into the system. Nuclei can drive wave formation by acting as pacemakers[13,14]. Modeling work demonstrates that the inclusion of pacemakers, whether explicitly or implicitly, drives waves at a frequency that correlates with pacemaker activity, with wave speed being dependent on this driving frequency[8,13,25–27]. Therefore, compartmentalizing the cytosol by introducing nuclei might affect how fast the system transitions from phase to trigger waves.

We supplement extracts with demembranated *Xenopus* sperm DNA (+XS), a method commonly used in the field to reconstitute nuclei[8,13–15,28]. A representative kymograph of this experiment shows clear wavefronts spanning the whole length of the tube (Fig. 3a, top). The zoomed-in region shows individual nuclei forming during interphase, importing active Cdk1 prior to NEB, and disappearing upon NEB (Fig. 3a, bottom). Even at this relatively coarse timescale (at 5-min time intervals), we observe the pacemaker nucleus accumulating more active Cdk1 than its neighbors and thereby undergoing NEB earlier
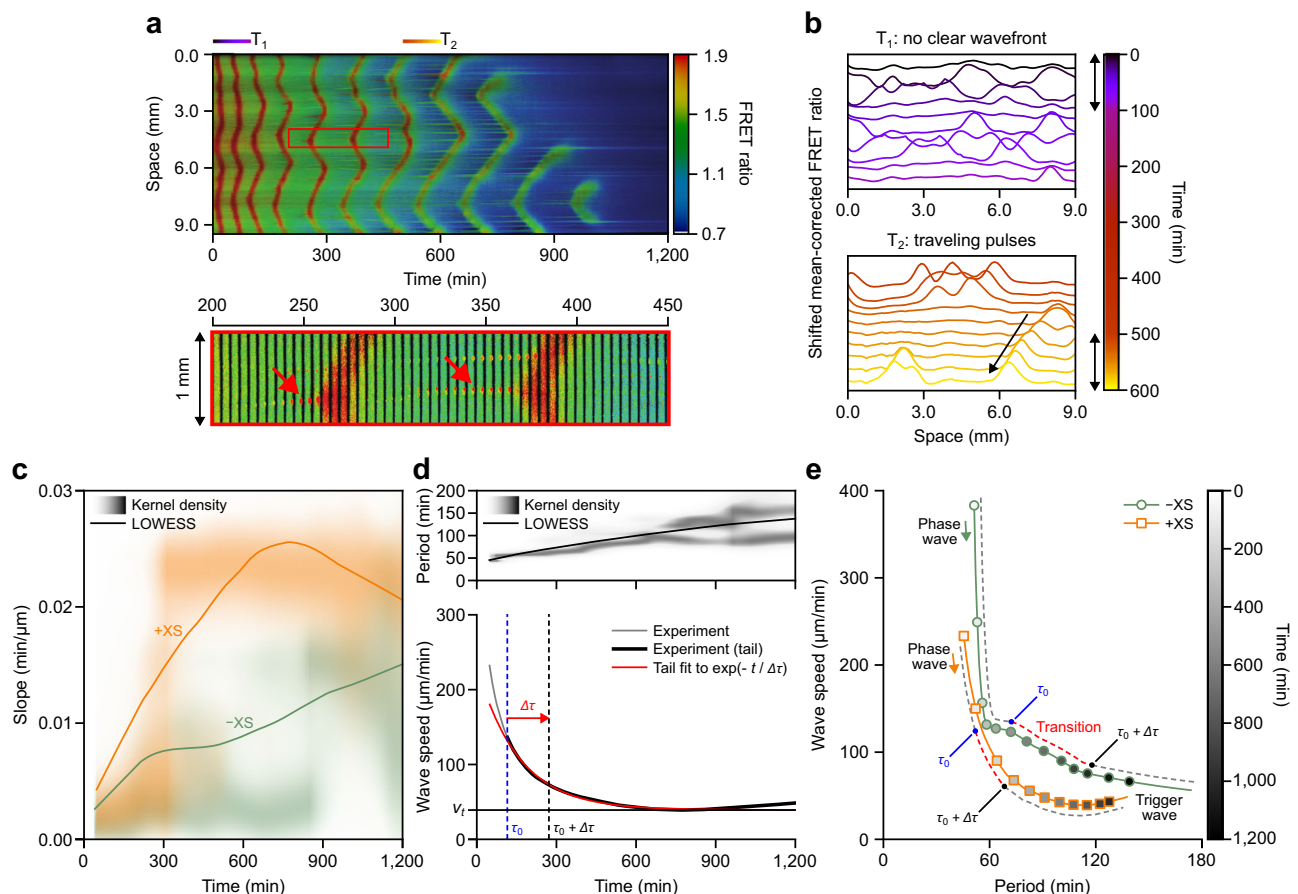
Fig. 3 | Nuclei entrain the system to the trigger wave regime. a Representative kymograph of the effects of adding sperm DNA (+XS). A magnified view of the region inside the red rectangle is provided in the lower panel to show nuclear growth before the entry into mitosis (red arrows). T_1 and T_2 mark the regions used in (**b**). **b** Comparison of shifted mean-corrected FRET ratio at early times with no clear wavefront (top) and distinctive traveling pulses at late times (bottom). **c** Comparison of the time dependence of the slope for the case of added sperm DNA (+XS, orange) and control (−XS, green). Kernel density estimations

(normalized at each time) and LOWESS curves are given in the corresponding colors. **d** Time evolution of the period (top) and wave speed (bottom) for +XS. **e** Speed-period relations for both conditions are obtained from LOWESS curves in Fig. 1d (−XS) and Fig. 3d (+XS), respectively. Open circles (−XS) and open squares (+XS) along the line highlight multiples of 100 min. The transition points are marked on dashed guides for each, as done previously. Data are pooled from two independent egg batches with three replicates each ($n = 6$).

(Fig. 3a, bottom, red arrows). After NEB, active Cdk1 fills the local region, and pulse-like waves propagate in both directions (Fig. 3a, bottom). Similar to the case without nuclei, the spatial profiles clearly indicate that at early times, the patterns resemble phase waves and at later times, trigger waves (Fig. 3b; Supplementary Movie 2). In other words, despite nuclei visibly forming at early times, we observe a comparable sweeping up of activity, though the effect is much noisier and punctuated by peaks associated with the nuclei themselves throughout the tube (Fig. 3b, top). As time progresses, trigger waves become dominant, and the system exhibits clear traveling pulses from the dominating pacemaker nucleus (Fig. 3b, bottom).

Repeating the same workflow described previously for this compartmentalized system, we find qualitatively similar behavior for each of the relevant quantities: the slope (Fig. 3c) and period (Fig. 3d, top) both increase over time, while the maximum activation rate remains constant (Supplementary Fig. 2c). Despite the time evolution of the period being similar between the two conditions (±XS), the slope for waves with nuclei consistently exceeds that of waves without nuclei within the 1200-min observation window (Fig. 3c), indicating a potential impact of nuclei on the wave propagation dynamics. To quantify this, we again measure the entrainment time from the exponential fitting (Fig. 3d, bottom). We obtain an entrainment time of $\tau_0 = 115$ min and $\Delta\tau = 157$ min, which is faster than that of the non-nuclei system, indicating an acceleration in the transition to trigger waves caused by the presence of nuclei. Interestingly, the fit for both conditions produces a terminal speed close to 40 µm/min, suggesting a common long-term behavior that agrees with speeds previously reported[8,13]. The difference in the entrainment time between the two systems is made clearer when considering the speed-period relation (Fig. 3e). As shown, the transient phase waves give way to trigger waves much more rapidly than in the systems without nuclei, as indicated by a decay in speed that begins earlier. The slight increase in speed at late times in the nuclei case is likely due to extract death. Despite this, it is clear that the addition of sperm DNA (nuclei) causes the system to admit trigger waves earlier in time, but also earlier in terms of period. This reinforces the idea that wave speed changes due to transient effects, rather than being driven by changes in period.

We then used modeling to test whether introducing spatial heterogeneities by phenomenologically incorporating nuclear import reproduces similar trigger wave dynamics. We added an import term to the model previously used (Eqs. (1) and (2)) that spatially modulates cyclin B-Cdk1 import according to a Gaussian profile (see Fig. 4a). This spatial domain around the nucleus is chosen to be approximately 150 µm, to approximate the size of the microtubule aster (Fig. 4a, width of the Gaussian profile; See Methods), motivated by previous studies[13,29]. Within this region, cell cycle regulators can be transported via molecular motors along microtubules and finally imported into the nucleus through nuclear pore complexes. Nuclear import is also modulated in time according to the Cdk1 activity at the nuclear location, such that during the mitotic phase, when the activity is high, import reduces to zero.

For a single nucleus, our numerical simulation shows that import allows for cyclin B-Cdk1 accumulation at the nuclear position while causing depletion in the surroundings. This difference in concentration leads to Cdk1 activation at the nucleus before its surroundings, thereby triggering a wave, as shown in Fig. 4b. Including different nuclei in the system at random positions and with different strengths and widths shows that nuclei act as pacemakers, quickly driving the system out of the phase wave regime and into the trigger wave regime (see Fig. 4c, Supplementary Movie 3). Interestingly, the model demonstrates the interaction between different nuclei. At long distances, the interaction is mediated via mitotic waves. At shorter distances, depletion of cyclin B-Cdk1 in the surroundings prevents the entry into mitosis of the nearby nuclei, which is instead triggered by an incoming wave.

Our results show that nuclei speed up the entrainment of the system to the trigger wave regime. Nuclei act as pacemakers[13,14], providing nucleation points for singular wavefronts. Supported by our computational analysis, we extend this notion to argue that the nuclei play a broader role in bringing the system out of the transitory, less-specified phase wave regime and into the well-defined, classical trigger wave regime. In systems without nuclei, patterns remain diffusive and exhibit fast speeds. Over time, trigger waves do develop, albeit slowly. Conversely, systems with nuclei develop trigger waves earlier and more frequently. Consequently, the former displays fast speeds that slowly decrease, while the latter displays speeds that quickly decay and follow a trigger wave speed-period relation.

External driving accelerates the transition to trigger waves

To further understand the entrainment of mitotic waves, we set out to drive waves explicitly by a cytostatic-factor (CSF) extract, similar to a previous study that drove an apoptotic signal through a tube of interphase extract using a reservoir of apoptotic-arrested extract[30].

CSF extract, a metaphase-arrested extract, is derived from inactivated eggs arrested at meiosis-II[31,32]. While the biological details of CSF arrest remain to be elucidated, the field largely agrees that the Emi family of proteins plays a major role by inhibiting APC/C, with other studies also highlighting the involvement of the Mos-MAPK pathway in CSF arrest[33,34]. Despite these uncertainties, CSF extracts consistently exhibit and maintain high Cdk1 activity unless released from arrest[35]. Moreover, these extracts can be frozen and stored for many months, providing a reliable source of stable high-Cdk1-activity extract[36]. Due to the self-promoting activity of Cdk1 in the mitotic circuit, supplementing oscillating extract with CSF is expected to result in forced activation and consequent propagation of traveling mitotic waves (Fig. 5a).

To validate this setup, we create a bistable traveling wave using CSF extracts and interphase extracts. Both extracts are prepared following standard protocols in the field[35–37]. We observe that briefly dipping an interphase-extract-filled tube into a CSF reservoir allows the high Cdk1 activity in CSF extracts to excite a traveling pulse of Cdk1 activity in the tube (Fig. 5b; Supplementary Movie 4). Waves propagate at a consistent speed of 40 ± 2 µm/min, in agreement with previously measured mitotic trigger waves in cycling extracts[8,13,14]. Visualizing the spatial profiles by shifting the FRET ratio reveals a clear traveling peak of activity, confirming the presence of trigger waves (Fig. 5c). This experiment demonstrates the efficacy of using CSF extracts as an explicit source to drive waves.

We thus applied the CSF extracts to drive tubes filled with cycling extract with or without sperm DNA added; in both cases, we observed the mitotic arrested region persistently drives multiple cycles of Cdk1 activity waves throughout the tube (Fig. 5d; Supplementary Movie 5 and 6). Similar to the non-driven experiments, wavefronts appear as pulses of high Cdk1 activity, regardless of the presence of nuclei, validating the emergence of trigger waves (Fig. 5e).

Applying the same analysis pipeline as before, we study how period and wave speed change over time. Initially, both conditions show a slight decrease in the oscillation period, likely due to the diffusing influence of CSF, followed by a typical period elongation (Supplementary Fig. 5a). While the observed behavior is qualitatively similar, the two conditions show a difference in the magnitude of the change in period despite experiencing the same driving force (Supplementary Fig. 5b). When measuring the wave speed in terms of slopes, we find that the system with nuclei has higher values than their non-nuclei counterparts (Supplementary Fig. 5c), matching what we observe in the non-driven system (Fig. 3c). This is likely due to the longer periods in the system with nuclei, but also suggests a possible difference at the level of wave propagation.

Our time scale analysis of wave speed reveals that the entrainment time for the condition with nuclei (+XS, $\tau_0 = 45$ min,
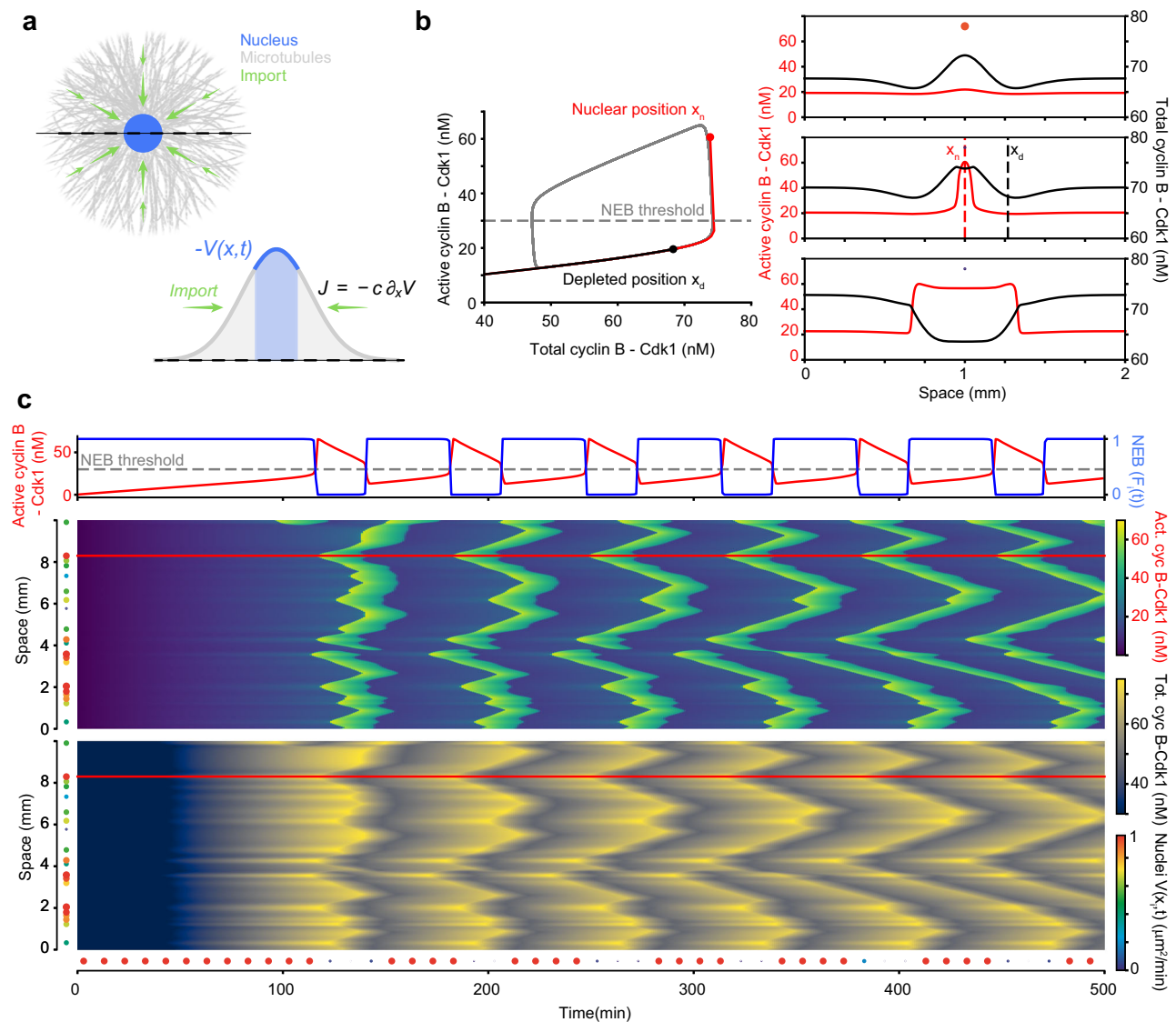
Fig. 4 | Nuclear localization of cyclin B-Cdk1 through import triggers mitotic waves. a Schematic representation of the nucleus (blue) and the surrounding microtubule structure (gray), which imports cell-cycle regulators such as cyclin B-Cdk1 via molecular motor transport, indicated with green arrows. The import strength is proportional to the concentration of cyclin B-Cdk1 (c) and is spatially described in the model by a Gaussian profile $V(x, t)$. The spatial derivative of this profile gives the direction of the flux J, which becomes zero during mitosis when local activity crosses the NEB threshold. **b** Time evolution of active (red) and total cyclin B-Cdk1 (black) in space (right panel), showing depletion of cyclin B in the neighborhood and its accumulation at the nuclear position (x_n) before activation. The accumulation of cyclin B triggers activation at the nuclear position before the surrounding areas, as indicated in the phase plane representation (left panel) at different positions. **c** Kymographs representing the spatiotemporal evolution of active (middle) and total (bottom) cyclin B-Cdk1 under the influence of nuclear import. The activation of import is shown in blue, relative to the activity at the position indicated in the kymograph (red, top). The strength of $V(x, t)$ and positions of nuclei x_i are represented at the boundaries according to the respective color scale.

$\Delta\tau = 81$ min) is shorter than without (−XS, $\tau_0 = 146$ min, $\Delta\tau = 396$ min) (Fig. 5f). The fact that entrainment times for driven waves are significantly shorter than their non-driven counterparts (Fig. 5f, ± XS, as compared to Fig. 3d, ± XS) seems to point to a cumulative effect from multiple pacemakers: both the CSF and nuclei contribute to entrainment. Interestingly, the entrainment time for the CSF-driven case without nuclei (−XS/+CSF, $\tau_0 = 146$ min, $\Delta\tau = 396$ min) is still longer than the undriven case with nuclei (+XS/−CSF, $\tau_0 = 115$ min, $\Delta\tau = 157$ min). It is plausible a set of multiple, but theoretically weaker, pacemakers could entrain the system faster given a distributed effect throughout space. In addition, the relaxation time scale for the CSF-driven case without nuclei ($\Delta\tau = 396$ min) is not shortened significantly compared to the non-driven experiment ($\Delta\tau = 526$ min), although CSF driving brings systems to initiate the transition more quickly ($\tau_0 = 146$ and 461 min, respectively). In

contrast, the presence of nuclei shortens both the initiation time and the relaxation time. This discrepancy underscores a fundamental biological difference in how CSF and nuclei contribute to entrainment, which is worth further investigation. Additionally, the fitted terminal speed 30 μm/min matches what we and others observed previously[8,13,14].

Importantly, driving the system in this way explicitly entrains the system to the trigger wave regime, quickly and permanently. The phase waves of early times start to transition to trigger waves within two or three cycles and propagate across the entirety of the tube. These waves appear to follow a clear speed-period relation, distinct from the undriven case (Fig. 5g). In both cases, we see a fast decrease in speed with small changes in the period that lead to a smooth approach to terminal speed (Fig. 5g). In this way, driving the system elucidates a clear difference between the transients—and possible phase waves—of
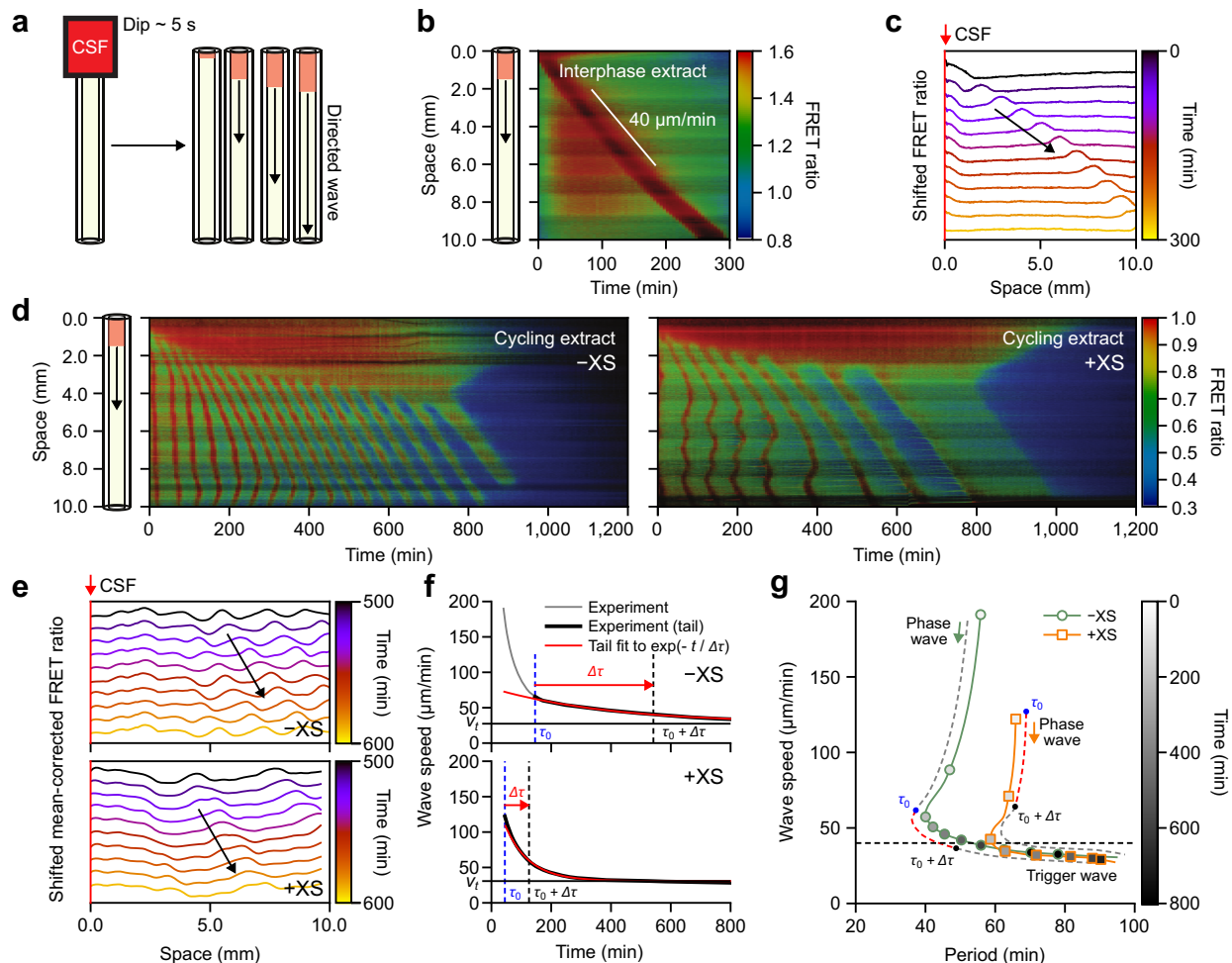
Fig. 5 | CSF boundary-driven mitotic waves. a Schematic representation of the experimental setup to trigger boundary-driven mitotic waves by a 5 second dip of an extract-filled tube in CSF extract. CSF-induced arrest is highlighted in red. **b** Solitary pulse of high Cdk1 activity propagating with a speed of 40 µm/min (wavefront indicated by a white line) in an interphase-arrested extract triggered by CSF dipping. **c** Spatial profiles of the shifted FRET ratio from the kymograph in (**b**) showing the excitable pulse. The red vertical line corresponds to CSF-induced arrest. **d** Kymographs for boundary-driven traveling waves in cycling extracts without (left, −XS) and with nuclei (right, +XS) present. **e** Traveling waves from kymographs in d revealed by the shifted mean-corrected FRET ratio without (−XS) and with nuclei (+XS). **f** Wave speed as a function of time for the two conditions in (**d**) analyzed via later-time exponential fits (red lines). **g** Speed-period relationship combining both LOWESS estimations for conditions with (+XS) and without (−XS) nuclei. Transition points and guides are as previously defined. Data are pooled from two independent egg batches with at least eight replicates each (n = 24 for −XS and n = 21 for +XS).

early times and trigger waves, and reinforces the notion of entrainment explicitly.

Spatial heterogeneities promote entrainment

There is a key conceptual distinction between phase waves and trigger waves. While information transmission by phase waves is nearly absent and synchrony is only maintained when the initial phase difference is small, trigger waves transmit information over long distances. The mechanisms underlying the two kinds of waves are also different. Although both appear in oscillatory systems, trigger waves require timescale separation and spatial coupling commonly mediated by diffusion. Timescale separation in our experiments is naturally present due to the rapid activation of cyclin B-Cdk1 compared to cyclin buildup from synthesis. It is this rapid activation that excites neighboring regions through protein diffusion and triggers a sustained propagation of the wave. In contrast, phase waves appear as a result of a small delay in the activation time of adjacent positions, creating a structured phase difference that takes the appearance of a wave. Another important difference is in the speed of the wave and its stability. The speed of a trigger wave is uniquely defined by the properties of the underlying oscillator and diffusion, and it is said to be stable because waves with

different propagation speeds will converge to the stable one. Conversely, a phase wave is not stable, it can appear at any speed, and diffusion will attenuate phase differences with time until the system oscillates synchronously.

We have previously demonstrated how trigger waves can be entrained by several ways of inducing spatial heterogeneity, such as increasing the spatial variability of cyclin B synthesis rate $k_s(x)$ (A_k, Fig. 2b–d), introducing nuclei pacemakers (Figs. 3, 4), and CSF-induced driving (Fig. 5). Here, to investigate the fundamental differences of trigger and phase waves, we use numerical simulations to initiate a trigger wave by introducing a period difference at the center of the spatial domain, a straightforward way of creating spatial heterogeneity without losing generality, and we assume spatially homogeneous levels of activity as the initial condition (Fig. 6a, (i)). Even under the influence of random noise, such period differences in space still result in clear trigger wavefronts and subsequent entrainment, as demonstrated in stochastic simulations to account for the stochastic nature of chemical reactions in embryos (Supplementary Fig. 6). In contrast, we initiate a phase wave by keeping the period fixed in space and asserting an initial condition where there is a linear difference in the phase of the oscillator that decreases as one moves far from the central position
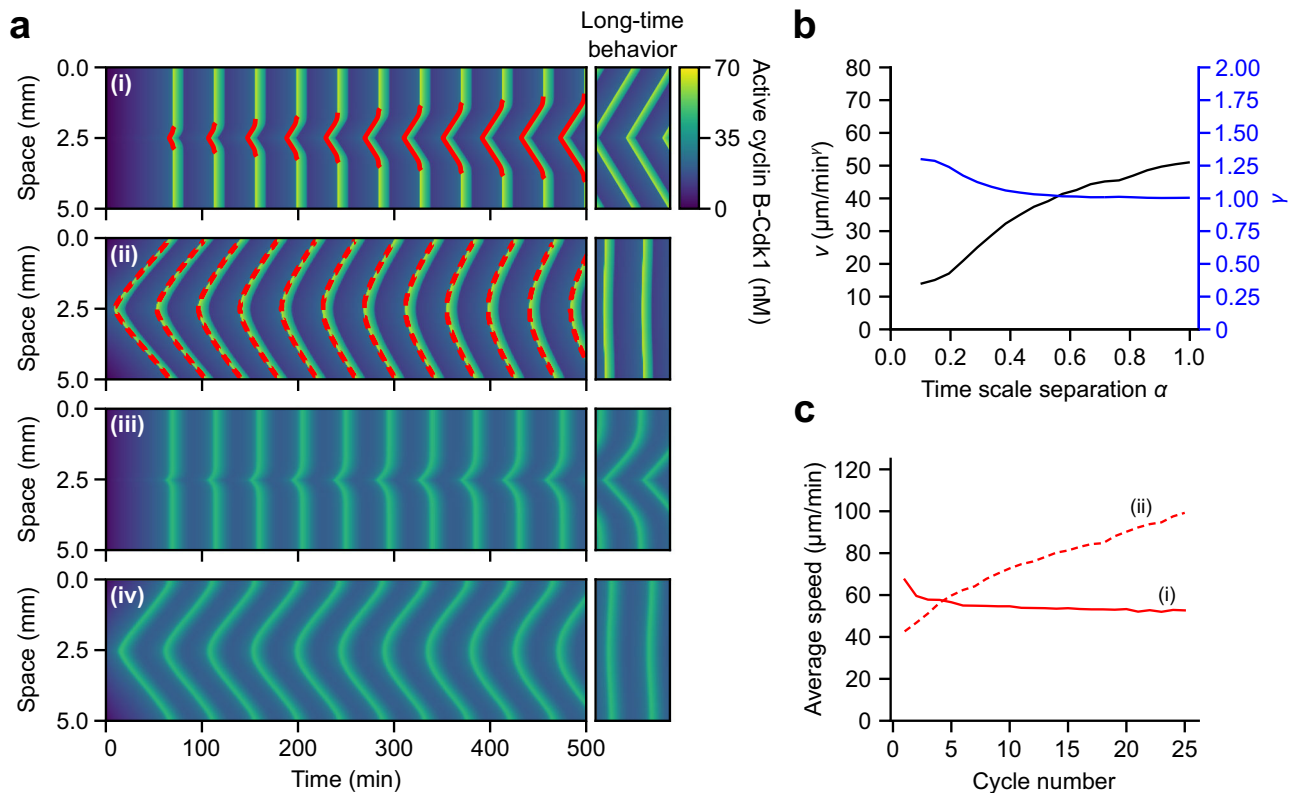
Fig. 6 | Influence of the oscillator properties and spatial heterogeneity on the formation of phase and trigger waves. a Kymographs representing the spatiotemporal evolution of cyclin B-Cdk1 activity. (i) Simulation with a spatially homogeneous initial condition of activity and a spatially heterogeneous period dependence to introduce a pacemaker at $x = 2.5$ mm, exhibiting trigger waves for $\alpha = 1$. (ii) Simulation with a spatially linear phase difference in the initial condition of activity and a spatially homogeneous period, exhibiting phase waves for $\alpha = 1$. (iii) Same spatial heterogeneity as (i) for $\alpha = 0.1$. (iv) Same spatial heterogeneity as (ii) for $\alpha = 0.1$. **b** v and γ as functions of α resulting from fitting the long-term shapes of pacemaker-driven waves in (**a**) with the expression $x = d + vt^\gamma$, showing a progressive transition to linearly propagating trigger waves ($\gamma = 1$) with a stable speed. **c** Temporal evolution with cycle number of the spatially averaged wave speed for phase and trigger waves in the shown kymographs (i) and (ii), (**a**). Speed is measured only at the wavefront segments indicated in red lines.

(Fig. 6a, (ii)). Then we explore the robustness of both systems by reducing the timescale separation of the oscillator (Fig. 6a, (iii, iv)), where the timescale separation is controlled by factor α for relaxation-like ($\alpha = 1$, Fig. 2a, left, black lines) and sinusoidal ($\alpha < 1$, Fig. 2a, left, red lines) oscillations. Quantifying the shapes of wavefronts at late times with the fit $x = d + vt^\gamma$, we obtain the dependence of the trigger-wave-likeness on α, summarized in Fig. 6b. We found that only when the oscillations are relaxation-like, indicated by larger values of α, do trigger waves establish in space in a stable manner, entraining the oscillatory background and displaying a linear front ($\gamma = 1$, Fig. 6a, (i)); in contrast, low values of α, which correspond to sinusoidal oscillations, lead to a curved front ($\gamma > 1$, Fig. 6a, (iii)). Increasing timescale separation with α also amplifies the penetration depth of the trigger wave into the medium[25,26], as shown in the long-time behavior, comparing Fig. 6a, (i) and (iii). On the other hand, phase waves do not change with the timescale separation, comparing Fig. 6a, (ii) and (iv). The spatially averaged wave speed, measured at the wavefront segments in the kymograph (Fig. 6a, (i), red lines), converges to the stable value expected for trigger waves (Fig. 6c, (i)); in contrast, the speed for phase waves (Fig. 6a, (ii), red lines) increases with time as the oscillations synchronize (Fig. 6c, (ii)).

Together, our numerical simulations (Figs. 2, 4, 6) suggest a crucial role of spatial heterogeneity in the phase-to-trigger wave transition, confirmed by our experimental observations, which we recapitulate in Fig. 7. First, disrupting oscillator homogeneity in space makes the system lose synchrony earlier in time (Fig. 7a). This acceleration is quantified in terms of the transition starting time τ_0. τ_0 is significantly reduced by introducing multiple nuclei in the

system (115 min, +XS), driving the system with CSF extract from the boundary (146 min, + CSF), or combining both of them (45 min, +XS/+CSF), compared to the control experiment (461 min, Control). The transition rate is also affected substantially by heterogeneity, particularly by nuclei (Fig. 7b). The slowdown of wave speed after τ_0 that approaches the terminal trigger wave speed is well characterized by an exponential decay with a time scale $\Delta\tau$ that varies across experimental conditions. $\Delta\tau$ is much shorter for extracts with nuclei (157 min for +XS and 81 min for +XS/+CSF) as opposed to cytoplasm-only experiments (396 min for +CSF and 526 min for Control), which signifies the important role of having multiple pacemakers in the entrainment.

Interestingly, despite the fact that spatial heterogeneity may cause one-order-of-magnitude changes both in τ_0 and $\Delta\tau$, the terminal speed across all conditions remains mostly unchanged (Fig. 7c). This suggests that regardless of the specific mechanism that drives the transition, coupled mitotic oscillators eventually synchronize with a consistent timing gradient established by trigger waves of 30–40 μm/min speed. A recent work by Huang et al. also highlighted the robustness of mitotic trigger wave speed under the physical stress of changing cytoplasmic concentrations[38]. Such a particular feature of being a reliable reference of timing distinguishes trigger waves from phase waves. In the absence of dynamic constraints imposed by diffusion, phase waves propagate at a fast but arbitrary speed that may depend on different physiological circumstances individual cells face. The speed of trigger waves, on the other hand, is a more intrinsic property of a dynamical system, as explored in our theoretical work (Fig. 6).
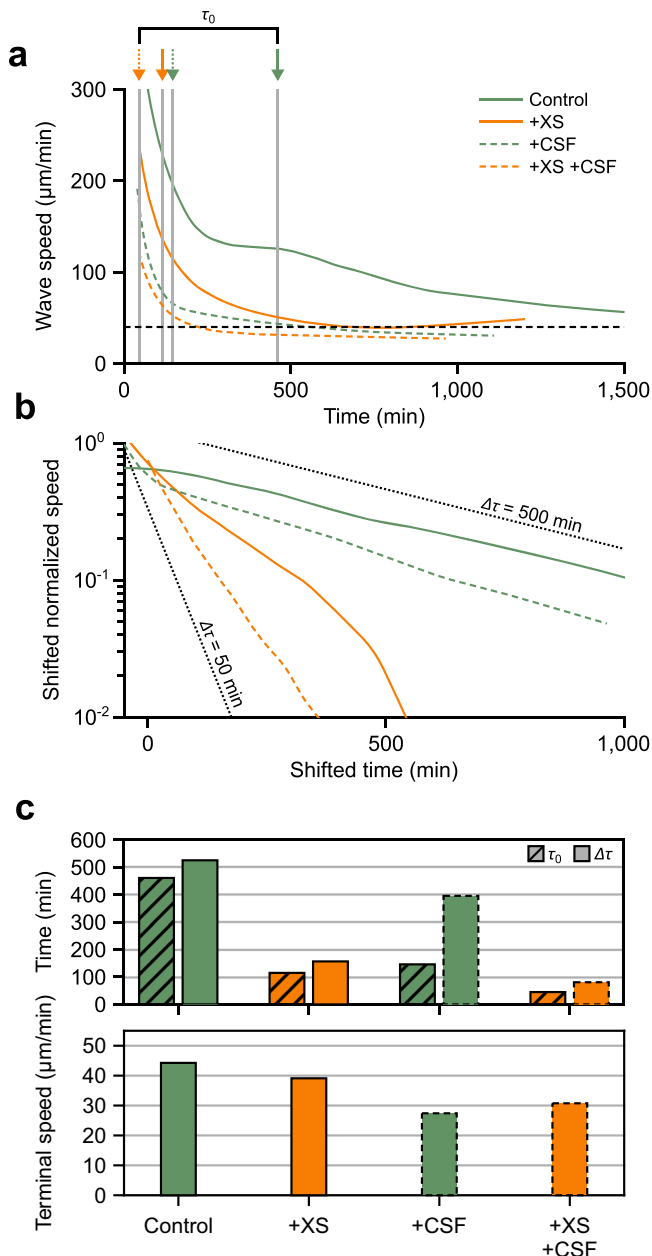
Fig. 7 | Spatial heterogeneity coordinates phase-to-trigger wave transition. **a** Time evolution of wave speed. Each vertical line with the corresponding arrow on the top indicates τ_0 for each experimental condition (461, 115, 146, and 45 min for Control, +XS, +CSF, and +XS/+CSF, respectively). The horizontal line depicts the terminal speed for the excitable system (40 μm/min). **b** Exponential relaxation of late-time wave speed. Time is measured from respective τ_0, and speed is offset by the terminal speed and then normalized against the speed at τ_0. The negative reciprocal of the curve slope gives a visual estimation of $\Delta\tau$, which are 526, 157, 396, and 81 min for each condition. Dotted guidelines correspond to 50 and 500-min time scale relaxations, respectively. **c** Transition time scales τ_0 and $\Delta\tau$ (top) and terminal speeds (bottom). Terminal speeds are 44, 39, 27, and 31 μm/min for each condition, converging to a similar level and comparable to the traveling speed of the activation pulse in interphase extracts driven by CSF (40 μm/min).

Discussion

Spatial coordination is essential to communicating complex biological processes. In this work, we probed the nature of one such coordination mechanism: mitotic waves that coordinate the process of cell division in large cells. Using a frog egg extract system which reproduces cell cycles in vitro, we characterized how mitosis spreads through the *Xenopus laevis* cytoplasm via either phase waves or trigger waves.

Although the properties of trigger waves in oscillatory systems have been thoroughly studied in the literature[25,26,39–43], their transient dynamics throughout many cycles and the mechanisms by which they transition into a stable attractor are less characterized. Through our frog egg extract experiments in thin long (quasi-one-dimensional) tubes, we observed phase waves in the transient dynamics towards the formation of a stable trigger wave. Even though cell cycle oscillations also slowed down, we showed that this is not required to observe a transition from phase waves to trigger waves. Certainly, it can take a long time before a pacemaker–a region that oscillates faster than its surroundings–is able to entrain its surroundings via trigger waves[25,26]. While in excitable media, a trigger wave can travel uninterrupted throughout the medium, in oscillatory media, the entrainment distance is limited by the inherent oscillatory period of its surroundings. Even in the transient time when a trigger wave is still forming, i.e. the first few cycles, the regular biochemical oscillations that drive the early embryonic cell cycle in *Xenopus laevis* will drive the whole system into mitosis throughout the whole medium. Any phase gradients will thus give rise to phase waves as the cell cycle phase is swept up.

This puts our work in dialogue with the existing literature regarding mitotic waves in *Drosophila*. Although period lengthening was found to be a driver of a sweep-to-trigger transition in *Drosophila*[19], we showed that this is not required for directing a transition from phase waves to trigger waves. Furthermore, this and other work highlight that phase wave properties are not robust to heterogeneity as they do not correspond to an actual attracting system solution. In Hayden et al.[19], the authors also show embryos displaying a nuclear density gradient in the syncytial embryo can lead to trigger rather than sweep or phase waves. We demonstrate a similar effect of disrupting homogeneity both by adding nuclei to the homogeneous system and by driving it explicitly with CSF. In all three cases, these trigger-wave-producing effects overtake the underlying quasi-synchronous patterns.

As phase waves do not actively propagate through a medium and require structured initial phase differences over a certain distance, they typically only persist for hundreds of micrometers. A trigger wave can travel long distances (~10 mm), and the typical length scale of the concentration gradient at the leading front ranges around hundreds of microns as well. This underscores the prevalence of phase waves in relatively small embryos, such as *Drosophila*, due to the limited length to accommodate a trigger wave front gradient. Indeed, when trigger waves are observed in *Drosophila*, their fronts (~200 μm wide) span roughly half the length of the embryo[18,19]. On the scale of some biological functions, the propagation distance of phase waves is relevant. However, for the specific purpose of coordination, this proves insufficient in larger cells. Trigger waves, as made evident by our work here, conversely, transmit signals orders of magnitude farther in distance. This questions the physiological relevance of phase waves in some systems. At most, one could imagine an evolutionary trade-off between speed and distance. For mitosis, it could be reasonable that nature would select for trigger waves in larger embryos such as *Xenopus*, where coordinating over large distances is more relevant than in *Drosophila*. Recently reported ultrafast waves[10,18,44,45], faster-than-trigger-wave signaling achieved without requiring bistable reactions or diffusion-mediated coupling, highlight the need for further comprehensive studies to understand why one organism favors one type of wave over another. Our work highlights the importance of examining not only stable waves but also the time evolution of waves as they develop. It also provides a framework that integrates experiments and theory to dissect the transition between different wave regimes.

Future experiments could expand on this work by pursuing other forms of perturbations by inhibiting the feedback loops in the network. The field already demonstrated the importance of Wee1 for forming the trigger[8], but with our setup and analysis framework, one

could quantify the effect and provide stronger evidence in either direction. The same applies to Cdc25, a phosphatase acting antagonistically to the Wee1 kinase in the regulation of Cdk1, both forming positive feedback loops with Cdk1. It would be interesting to observe whether Wee1 and Cdc25 affect this time dependence in similar manners. Moreover, we know that these inputs also translocate in and out of the nucleus throughout one cycle, at different times[46,47]. It stands to reason that inhibition thereof could change in the presence of nuclei, and thus, we might see a nuclei-dependent effect on how inhibition perturbs this transition[28]. Moreover, one main difference between our work in vitro and the in vivo context of *Xenopus* is the number of nuclei. Here, we probe dynamics in the context of many nuclei in a shared cytoplasm: a pseudo-syncytial system. For the *Xenopus* embryo, the first cycle contains a single nucleus. It is possible the situation is reversed in that case. A single strong pacemaker initiates a trigger wave that eventually decays after several cell cleavages. In smaller cells, diffusive mixing becomes the dominant process for synchronizing mitosis, rather than trigger waves[11]. Clearly, much work remains on elucidating the details of time-dependent wave behavior.

In another vein, the CSF driving setup could be used to expand on this study by asking how perturbations to the clock network, including inhibitions for other clock constituents such as Cdc25, Wee1, PP2A, etc., change trigger wave propagation. Furthermore, like CSF extracts, interphase extracts maintain activity for months while frozen, making them more accessible for faster and simpler data acquisition than involving the cycling system. In practice, such experiments could provide a more straightforward method for testing all of the perturbations mentioned above: clock inhibitors, glycerol-modulated diffusion, etc. In particular, this would facilitate a direct examination of whether nuclei indeed perturb wave propagation as it would eliminate their dual role as a pacemaker. In total, this setup offers a wealth of opportunities to probe trigger wave dynamics, relevant for in vivo embryogenesis in *Xenopus*.

Moreover, one can envision perturbing the source itself. Theory predicts the wave speed to depend on the difference between the pacemaker and bulk frequency[25,26]. Modulating the driving force of the CSF source, whether through dilution or the use of inhibitors, can provide a direct test of these theoretical predictions. As the interplay between CSF arrest and its driving force remains unclear, comprehending such perturbations requires additional modeling efforts. Nevertheless, our successful demonstration of driving waves in vitro underscores the significance of elucidating these interactions. Taken together, these future investigations would not only enhance our understanding of how organisms transmit mitotic information across long distances, but also provide fundamental insights into the nature of biochemical waves generally, and phase waves and trigger waves in particular.

Methods

Xenopus laevis egg extracts

All experiments and animal procedures were conducted in compliance with ethical regulations and the description in the Institutional Animal Care and Use Committee (IACUC) approved protocol (#PRO00011571) at the University of Michigan-Ann Arbor. To capture mitotic waves in vitro, we made cell-free cycling extracts from *Xenopus laevis* eggs following a published protocol[20,21] adapted from Murray[32]. Female *Xenopus laevis* frogs were provided by Nasco or Xenopus 1. All frogs were > 3 years old. A total of five frogs were primed for ovulation with an injection of 100 IU of human chorionic gonadotropin (HCG; MP Biomedicals, 2198591) 1–2 weeks before and then induced with 600 IU HCG the night before experiments. Collected eggs were swirled in a dejellying solution (100 mM KCl, 0.1 mM CaCl$_2$, 1 mM MgCl$_2$ and 2% w/v cysteine (Sigma-Aldrich, C7352)) and then activated using 0.5 µg/mL calcium ionophore A23187 (MilliporeSigma, C7522) for roughly 2–5 min. The eggs were then washed with 0.2x Marc's modified

Ringer's (MMR; 100 mM NaCl, 2 mM KCl, 1 mM MgCl$_2$, 2 mM CaCl$_2$, 0.1 mM EDTA and 5 mM HEPES, pH 7.8) to stop activation and then extract buffer (EB; 100 mM KCl, 1 mM MgCl$_2$, 0.1 mM CaCl$_2$, 50 nM sucrose and 10 mM HEPES, pH 7.8). Following these washes, the eggs were subsequently washed with EB supplemented with three protein inhibitors (PI3; 10 µg/mL each of leupeptin (Sigma-Aldrich, L2023), pepstatin (Sigma-Aldrich, P5318) and chymostatin (Sigma-Aldrich, C7268)). Eggs were transferred to centrifuge tubes filled with EB + PI3 and 100 µg/mL cytochalasin B (MP Biomedicals, 2195119). The egg-filled tubes were then packed and centrifuged for 10 min and then 5 min at 20,000g and 4 °C using a Beckman Avanti J-E Centrifuge with a JS-13.1 swinging bucket rotor to extract cytosolic materials. The PI3 and cytochalasin B mixture was added to the cytosolic fraction to a final concentration of 10 µg/mL.

Extracts were then supplemented with the Cdk1-FRET sensor and sperm DNA, depending on the experimental conditions. The Cdk1-FRET sensor was prepared as described in Maryu and Yang[15]. Demembranated sperm DNA was prepared following the established protocol[32]. In brief, DNA was extracted from male frog testes postmortem. The sperm DNA was demembranated by soaking the testes in a mixture of nuclear preparation buffer (NPB; 250 mM sucrose, 15 mM HEPES, 1 mM EDTA, 0.5 mM spermidine trihydrochloride (Sigma-Aldrich, S2501), 0.2 mM spermine tetrahydrochloride (Sigma-Aldrich, S1141), 1 mM dithiothreitol (Sigma-Aldrich, D0632), 10 µg/mL leupeptin and 0.3 mM PMSF) and 10 mg/mL lysophosphatidylcholine (Sigma-Aldrich, L4129). The sperm was washed with NPB and 0.3% bovine serum albumin (BSA; Sigma-Aldrich, A-7906) and then frozen, suspended in NPB, BSA and 30% w/v glycerol.

Work from the Yang lab demonstrated an intermediate range of dilution of the extracts can improve the number of cycles, with the best activity at around 20% dilution[48]. As a result, for the data described here, the dilution was kept constant at 20% with EB. Extracts were subsequently loaded into 5–10 mm-long sections of Teflon-coated Masterflex PTFE tubing (inner diameter 150 µm; ColeParmer, EW-06417-74) via aspiration, submerged under mineral oil (Macron Fine Chemicals, MK635704) on a glass-bottom dish (WillCo Wells, GWST-5040). Given the dimensions of the tubing used, tubes were organized into, at most, groups of five in one direction. We did not observe any significant contamination between tubes, even when forcing them into such close proximity. Images were acquired using epifluorescence microscopy using an inverted microscope (Olympus IX-83) equipped with a UPlanSApo 4x (NA 0.16, Olympus) objective, ORCA-Flash4.0 V3Digital CMOS camera (Hamamatsu), X-Cite Xylis Broad Spectrum LED Illumination System (Exelitas Technologies Corp.) and a motorized XY stage (Prior Scientific Inc.) controlled by µManager[49]. Images were acquired for up to 2 days at 0.2 frame/min.

For Fig. 5b, c, frozen interphase extracts were made using the standard protocol in the field[24,37]. This process was similar to the cycling extract protocol, with the following changes. In addition to PI3 and cytochalasin B, 10 mg/mL cyclohexamide (Sigma-Aldrich, C7698) was added. Once the cytosolic fraction was obtained, it was aliquoted and frozen at −80 °C until needed. On the day of the experiment, one aliquot is thawed on ice, supplemented with reporters, and then loaded into PTFE tubing for imaging.

The CSF extracts were made following established protocols[35] adapted from the original[32]. This process was largely similar to the cycling extract protocol, with the following changes. Eggs were not activated. In addition to washes with EB, the eggs were also washed with CSF-XB (100 mM KCl, 0.1 mM CaCl$_2$, 2 mM MgCl$_2$, 10 mM HEPES, 50 mM sucrose and 5 mM EGTA, pH 7.7). In addition, cytochalasin D was used in place of cytochalasin B. Using laid eggs, we produced large quantities of extract (on the order of mL), vastly more than necessary for a single experiment (10–20 µL). To preserve said large quantities of extract, we implemented a freezing protocol adopted from Takagi and Shimamoto[36]. Prepared extracts were loaded into centrifugal filters

(Millipore, UFC801024) and spun at 17,000g for 10 min at 4 °C. The filters were then placed upside down in collection tubes and spun at a slower rate of 2000g for 10 s. The separated fractions were each transferred to individual tubes in small quantities (-50 μL). These tubes were rapidly cooled to frozen in a −80 °C freezer. On the day of experiment, the separate fractions were thawed and combined, using a pipette to mix. To maintain conditions across the reservoir and the cycling extract, CSF extracts were also diluted to 20% with extract buffer. No reporters or drugs were added to these extracts.

In order to set up the CSF-driven system, we first cut PTFE tubing into individual sections of -10 mm lengths and loaded each via aspiration such that the extract (either interphase or cycling extracts) filled the tube in excess: visual inspection of the syringe adapter showed the fluid line exceeding the tube opening. Then the tube was dipped into the CSF reservoir syringe-end first for 5–10 s to ensure fluidic contact between the cycling/interphase and CSF extracts. While the original apoptotic wave paper[30] described maintaining contact between the reservoir and tubes for many minutes, we observed any contact longer than -10 s resulted in mitotic arrest overtaking most, if not all, of the tube. This sometimes occurred even at shorter dipping times. As such, care was taken to minimize the contact time. Tubes were then submerged under mineral oil and imaged as discussed above.

Image processing and analysis methods

Grids of images were captured and subsequently stitched together using ImageJ's Grid/Pairwise Stitching plug-in[50], in conjunction with additional pipeline code written in Fiji/Java (for handling multiple folders of images). Bright-field images from the first frame were used to generate stitching parameters, which were fed to ImageJ to stitch each channel at each frame consecutively. While capturing grids of images in this way resulted in a non-zero time lag between subsequent sections along a tube, and multiple of this lag between the first and last sections, this gap amounted to a few seconds, much smaller than the scale of the overall imaging timestep which was on the order of minutes. As such, this was ignored for the purposes of analysis. The stitched stacks were then straightened using Fiji and a manually selected curve from the tube edge in the bright-field images as an input. This curve was unique to each tube, though the profiles of the tubing sections often followed roughly the same shape, without much distortion. Afterwards, the tube images were cropped so as to only include the inner dimension, again using the bright-field images as a guide. Additionally, the FRET ratio was calculated separately as in Maryu and Yang[15].

For the analysis of wavefronts, first, individual kymographs were corrected for any decaying baseline trend, and any NaN pixels were filled using the scikit-image function `inpaint`. Afterwards, we detected peaks for each time series at each pixel along the tube. The peaks themselves were then clustered into individual cycles in Python. Once cycles were identified and separated, the collection(s) of peaks were fitted and/or smoothed in space and time, after which slopes (and speeds) were calculated along each front by taking the numerical derivative of the fits at each point. Periods followed directly from the detected peaks. The normalized density estimation for the time dependence of the period, slope, and maximum activation rate made use of the SciPy function `scipy.stats.gaussian_kde` using a Gaussian kernel of $\sigma_t = 50$ min as a sliding window for time and the maximum value normalized to one.

Moving horizon fitting

To determine τ_0, we examined the quality of the exponential fitting of the wave speed's later-time decay, by calculating mean square residual (MSR) of the fitting for the time frame $[\tau_0, \infty)$. Both the MSR (Supplementary Fig. 1, top) and its derivative with respect to τ (Supplementary Fig. 1, bottom) sharply changed (Control, +XS, and +CSF) at a finite τ indicating the fitting at the tail segment abruptly worsened upon

extending it to earlier times. τ_0 was defined as the largest time that the derivative lies below a chosen threshold, $-0.025\,\mu\text{m}^2/\text{min}^3$ (horizontal red line). τ_0 was affected minimally by the choice of the threshold due to the sharp change in the derivative. This definition applied consistently across data with varying fitting quality (for example, +XS data has an overall lower fitting quality than +XS/+CSF data), making it preferable over other thresholding methods based solely on MSR. If the fitting quality is good for all scanned τ values (in the case of +XS/+CSF), the earliest recorded time was defined as τ_0.

Mathematical model

We use the mathematical model previously introduced[8,24] describing the dynamics of the total cyclin B-Cdk1 $c \equiv c(x, t)$ and its active form $a \equiv a(x, t)$. The equations can be written in the following form

$$\partial_t c = \eta\beta(k_s - h_{\text{Deg}}(a)c) + D\nabla^2 c + \nabla \cdot (c\nabla V), \tag{1}$$

$$\partial_t a = \eta[\alpha(h_{\text{Cdc25}}(a)(c - a) - h_{\text{Wee1}}(a)a) + \beta(k_s - h_{\text{Deg}}(a)a)] + D\nabla^2 a + \nabla \cdot (a\nabla V), \tag{2}$$

where the newly introduced dimensionless parameters are α, β, and η. $V \equiv V(x, t)$ describes the influence of nuclei as detailed below. The parameter η scales all rate constants and allows for precise control of the period of the oscillations. The parameter α scales the rates related to activation−inactivation processes mediated by Cdc25 phosphatase and Wee1 kinase, which are described by Hill equations of the form

$$h_{\text{Cdc25}}(a) = a_{\text{Cdc25}} + \frac{b_{\text{Cdc25}}a^{n_{\text{Cdc25}}}}{\text{EC}_{50,\text{Cdc25}}^{n_{\text{Cdc25}}} + a^{n_{\text{Cdc25}}}}, \tag{3}$$

$$h_{\text{Wee1}}(a) = a_{\text{Wee1}} + \frac{b_{\text{Wee1}}\text{EC}_{50,\text{Wee1}}^{n_{\text{Wee1}}}}{\text{EC}_{50,\text{Wee1}}^{n_{\text{Wee1}}} + a^{n_{\text{Wee1}}}}. \tag{4}$$

The parameter β scales synthesis and degradation rates to control the time spent in interphase and mitosis. The degradation term encompasses the APC/C-induced degradation of cyclin B which is described with the Hill equation

$$h_{\text{Deg}}(a) = a_{\text{Deg}} + \frac{b_{\text{Deg}}a^{n_{\text{Deg}}}}{\text{EC}_{50,\text{Deg}}^{n_{\text{Deg}}} + a^{n_{\text{Deg}}}}. \tag{5}$$

The parameters of the model are $k_s = 1.5\,\text{nM/min}$, $a_{\text{Cdc25}} = 0.8\,\text{min}^{-1}$, $b_{\text{Cdc25}} = 4\,\text{min}^{-1}$, $\text{EC}_{50,\text{Cdc25}} = 35\text{nM}$, $n_{\text{Cdc25}} = 11$, $a_{\text{Wee1}} = 0.4\,\text{min}^{-1}$, $b_{\text{Wee1}} = 2\,\text{min}^{-1}$, $\text{EC}_{50,\text{Wee1}} = 30\text{nM}$, $n_{\text{Wee1}} = 3.5$, $a_{\text{Deg}} = 0.01\,\text{min}^{-1}$, $b_{\text{Deg}} = 0.06\,\text{min}^{-1}$, $\text{EC}_{50,\text{Deg}} = 32\text{nM}$, $n_{\text{Deg}} = 17$, $\alpha = \beta = \eta = 1$, $D = 240\,\mu\text{m}^2/\text{min}$ and are kept constant in this work otherwise specified.

The influence of nuclei in the dynamics is incorporated using the variable $V(x, t)$, which describes the import strength of cyclin B-Cdk1 into the nucleus. It accounts for the balance of import and export processes due to molecular motors transporting cargo through the cytoskeleton and directing import through the nuclear envelope. We adopt $V(x, t)$ expressed as below in terms of separable functions, each accounting for the contribution of a single nucleus to the processes,

$$V(x, t) = \sum_{i=1}^{N} F_i(t)G_i(x), \tag{6}$$

where N is the number of nuclei. In the absence of nuclei, $V(x, t) = 0$. The time-dependent factor

$$F_i(t) = F(a(x_i, t)) = \frac{\text{EC}_{50,\text{NEB}}^{n_{\text{NEB}}}}{\text{EC}_{50,\text{NEB}}^{n_{\text{NEB}}} + a^{n_{\text{NEB}}}}. \tag{7}$$

constitutes an ultrasensitive switch-like response of the dynamics to the local Cdk1 activity at the fixed position of the i-th nucleus x_i. The spatial component is described by a Gaussian profile for simplicity given by

$$G_i(x) = -\epsilon_i e^{-\frac{(x-x_i)^2}{2\sigma_i^2}}, \tag{8}$$

where x_i, ϵ_i, and σ_i are the parameters of each single nucleus. The parameter ϵ_i defines their import strength and σ_i the typical size of the microtubule aster. The positions x_i of the nuclei are randomly distributed in the spatial domain, their import strengths ϵ_i are randomly sampled using a normal distribution of mean 120 μm^2/min and standard deviation 72 μm^2/min. The parameter σ_i is again normally distributed with mean 150 μm and standard deviation 30 μm. $EC_{50,NEB} = 30$ nM and $n_{NEB} = 20$.

Numerical simulations

The model described by Eqs. (1) and (2) is a system of two coupled partial differential equations integrated in time with a pseudo-spectral method[51]. We consider a grid with N_x grid points to describe a spatial domain of length L_x with no-flux boundary conditions and we integrate with a timestep Δt the linear terms in Fourier space exactly, while the nonlinear terms are integrated using a second-order in time approximation.

Numerical simulations showing the transition from phase to trigger waves in time (Fig. 2b–e) are performed using the integration parameters $N_x = 4096$, $L_x = 10$ mm, and $\Delta t = 0.002$ min, starting with initial conditions $a(x) = c(x) = 0$ nM. Spatial heterogeneity is taken into consideration with the position-dependent synthesis term given as the following form: $k_s(x) = k_s[1 + \Theta(x) + A_k N(x)]$, where $\Theta(x)$ is a predefined heterogeneity profile, which is mainly to induce pacemakers at chosen locations, and A_k defines the amplitude of the quenched random parameter profile $N(x)$. $k_s(x)$ is set to zero for simulations presented in Fig. 2. For the random profile $N(x)$, we first generated colored noise $n(x) = F^{-1}[\exp(-(\sigma k)^2/2 - 2i\pi u_k)](x)$ using the inverse Fourier transform F^{-1} with u_k for each Fourier mode k being a random number uniformly distributed between 0 and 1. The typical length scale σ of the spatial heterogeneity is chosen to be 77.46 μm. $n(x)$ is normalized based on the following expression to obtain $N(x)$.

$$N(x) = \frac{n(x) - \int_0^{L_x} n(x)\mathrm{d}x/L_x}{\max[n(x) - \int_0^{L_x} n(x)\mathrm{d}x/L_x]}. \tag{9}$$

For results presented in Fig. 2, we assume the time dependence of the parameter $\beta(t)$ (Fig. 2a, top), which is inferred from the observed time-dependence of the period (Fig. 1d, top). The time dependence is considered after the completion of the first cycles, at which the period measurement becomes available in the experimental setting.

Numerical simulations including the nuclear import (Fig. 4b, c) are performed using the integration parameters $N_x = 4096$, $L_x = 10$ mm, and $\Delta t = 0.002$ min, with the same uniform initial conditions.

Simulations that are driven by pacemakers, which include panels (i) and (iii) of Fig. 6a, are performed using the integration parameters $N_x = 1024$, $L_x = 5$ mm, and $\Delta t = 0.002$ min, with initial conditions $a(x) = c(x) = 0$ nM and a pacemaker located at $x = 2.5$ mm. The pacemaker is parameterized in terms of the rectangular profile $\Theta(x) = \Delta\Theta H(s/2 - |x - L_x/2|)$, where $\Delta\Theta = 0.3$, $H(x)$ is the Heaviside function, and $s = 50$ μm. Simulations showing fading phase waves, which include panels (ii) and (iv) of Fig. 6a, use a constant value of $\Theta(x)$ and initial conditions $a(x) = a_{max}(1 - 2|x - L_x/2|/L_x)$ with $a_{max} = 20$ nM and $c(x) = 0$ nM.

Stochastic simulations

We use Gillespie's stochastic simulation algorithm[52] (SSA) to assess whether the consideration of intrinsic stochasticity of biochemical reactions could have a remarkable impact on the wave dynamics observed in numerical simulations. $V_c = 1$ pL is chosen as the benchmark reaction volume for the SSA, below which the chemical species is assumed to be well-mixed in space. The characteristic time scale T_c of reactions involved in mitotic circuits is of the order of $10^{-1}–10^1$ min, which is obtained from the reciprocals of the reaction rate constants. Together with the diffusion constant D of macromolecules, it defines the characteristic length scale of diffusion, $\sqrt{DT_c} \sim 10^0 - 10^2$ μm. $V_c = 1$ pL is taken as the lowest estimate of the volume corresponding to the length scale, which allows us to investigate the largest possible intrinsic fluctuations of dynamics. Following the formalism summarized in detail by Guan et al.[21], Eqs. (1) and (2) are rephrased into a master equation describing Markov jump processes in two-dimensional molecule number space. Realizations of stochastic trajectories are obtained using a solver for discrete stochastic processes implemented in `DifferentialEquations.jl`[53], with the same parameter sets as specified in the previous section.

To test the effect of extrinsic stochasticity on the entrainment, we modified Eqs. (1) and (2) into a system of Langevin equations with additive Gaussian noise ξ as

$$\partial_t c = \eta\beta(k_s - h_{Deg}(a)c) + D\nabla^2 c + \xi_c(x,t), \tag{10}$$

$$\partial_t a = \eta[\alpha(h_{Cdc25}(a)(c-a) - h_{Wee1}(a)a) + \beta(k_s - h_{Deg}(a)a)] + D\nabla^2 a + \xi_a(x,t), \tag{11}$$

where the noise has zero mean and is correlated as $\langle\xi_i(x,t)\xi_j(x',t')\rangle = 2S\delta_{ij}f(x,x')\delta(t-t')$. $f(x,x') = 1$ if both points belong to the same discretization grid and 0 otherwise. Unlike intrinsic stochasticity whose degree of fluctuation is determined by the system size and specific modes of associated chemical reactions, the noise introduced by extrinsic stochasticity can be arbitrarily large and may alter the wave dynamics significantly. Thus, we explore a broad range of the stochasticity level S, including the conditions exhibiting much more pronounced fluctuations than the SSA results. We use the same numerical discretization as described for the deterministic simulation ($N_x = 1024$), such that the volume of each grid point is of the order of V_c. The equations are integrated using a stochastic integration algorithm implemented in `DifferentialEquations.jl` (SOSRA)[53].

Statistics and reproducibility

Experiments measuring cell cycle dynamics and wave speeds in the undriven system with and without added sperm DNA (XS) (Figs. 1, 3) were conducted with two independent *Xenopus* eggs batches with three replicates each. Experiments measuring cell cycle dynamics and wave speeds in the driven system with and without XS (Fig. 5) were conducted with two independent egg batches with eight or more independent samples. Simulations to assess the influence of spatial heterogeneity (Fig. 2e) were performed as previously described. For each A_k, we averaged the results over 10 realizations of the spatial heterogeneity, as defined by Eq. (9). No experiment was excluded from any subsequent analysis. Statistical power calculations were not used in determining the sample size prior to conducting experiments. None of the investigators were blinded to sample preparation or allocation during experiments, nor analysis and interpretation.

Reporting summary

Further information on research design is available in the Nature Portfolio Reporting Summary linked to this article.

Data availability

The authors declare that the data supporting the findings of this study are available within the paper and its supplementary information files. The data generated in this study have been deposited in the Zenodo database under accession code: https://doi.org/10.5281/zenodo.10583185[54]. Source data are provided with this paper.

Code availability

Python codes for the analysis of mitotic waves properties and Fortran codes for performing numerical simulations are deposited on GitHub. These codes are available from Zenodo: https://doi.org/10.5281/zenodo.10583185[54].

References

1. Novak, B. & Tyson, J. J. Numerical analysis of a comprehensive model of M-phase control in *Xenopus* oocyte extracts and intact embryos. *J. Cell Sci.* **106**, 1153–1168 (1993).
2. Novak, B. & Tyson, J. J. Modeling the cell division cycle: M-phase trigger, oscillations, and size control. *J. Theor. Biol.* **165**, 101–134 (1993).
3. Morgan, D. O. *The Cell Cycle: Principles of Control* (New Science Press, 2007).
4. Foe, V. E. & Alberts, B. M. Studies of nuclear and cytoplasmic behaviour during the five mitotic cycles that precede gastrulation in *Drosophila* embryogenesis. *J. Cell Sci.* **61**, 31–70 (1983).
5. Hara, K., Tydeman, P. & Kirschner, M. A cytoplasmic clock with the same period as the division cycle in *Xenopus* eggs. *Proc. Natl Acad. Sci.* **77**, 462–466 (1980).
6. Farrell, J. A. & O'Farrell, P. H. From egg to gastrula: how the cell cycle is remodeled during the *Drosophila* mid-blastula transition. *Annu. Rev. Genet.* **48**, 269–294 (2014).
7. Anderson, G. A., Gelens, L., Baker, J. C. & Ferrell, J. E. Desynchronizing embryonic cell division waves reveals the robustness of *Xenopus laevis* development. *Cell Rep.* **21**, 37–46 (2017).
8. Chang, J. B. & Ferrell Jr, J. E. Mitotic trigger waves and the spatial coordination of the *Xenopus* cell cycle. *Nature* **500**, 603–607 (2013).
9. Deneke, V. E., Melbinger, A., Vergassola, M. & Di Talia, S. Waves of Cdk1 activity in S phase synchronize the cell cycle in *Drosophila* embryos. *Dev. Cell* **38**, 399–412 (2016).
10. Deneke, V. E. & Di Talia, S. Chemical waves in cell and developmental biology. *J. Cell Biol.* **217**, 1193–1204 (2018).
11. Gelens, L., Anderson, G. A. & Ferrell Jr, J. E. Spatial trigger waves: positive feedback gets you a long way. *Mol. Biol. Cell* **25**, 3486–3493 (2014).
12. Di Talia, S. & Vergassola, M. Waves in embryonic development. *Annu. Rev. Biophys.* **51**, 327–353 (2022).
13. Nolet, F. E. et al. Nuclei determine the spatial origin of mitotic waves. *eLife* **9**, e52868 (2020).
14. Afanzar, O., Buss, G. K., Stearns, T. & Ferrell Jr, J. E. The nucleus serves as the pacemaker for the cell cycle. *eLife* **9**, e59989 (2020).
15. Maryu, G. & Yang, Q. Nuclear-cytoplasmic compartmentalization of cyclin B1-Cdk1 promotes robust timing of mitotic events. *Cell Rep.* 41 (2022).
16. Bischof, J. et al. A cdk1 gradient guides surface contraction waves in oocytes. *Nat. Commun.* **8**, 849 (2017).
17. Rankin, S. & Kirschner, M. The surface contraction waves of *Xenopus* eggs reflect the metachronous cell-cycle state of the cytoplasm. *Curr. Biol.* **7**, 451–454 (1997).
18. Vergassola, M., Deneke, V. E. & Di Talia, S. Mitotic waves in the early embryogenesis of *Drosophila*: bistability traded for speed. *Proc. Natl Acad. Sci.* **115**, E2165–E2174 (2018).
19. Hayden, L., Hur, W., Vergassola, M. & Di Talia, S. Manipulating the nature of embryonic mitotic waves. *Curr. Biol.* **32**, 4989–4996 (2022).
20. Guan, Y. et al. A robust and tunable mitotic oscillator in artificial cells. *eLife* **7**, e33549 (2018).
21. Guan, Y., Wang, S., Jin, M., Xu, H. & Yang, Q. Reconstitution of cell-cycle oscillations in microemulsions of cell-free *Xenopus* egg extracts. *J. Vis. Exp.* **139**, e58240 (2018).
22. Sun, M., Li, Z., Wang, S., Maryu, G. & Yang, Q. Building dynamic cellular machineries in droplet-based artificial cells with single-droplet tracking and analysis. *Anal. Chem.* **91**, 9813–9818 (2019).
23. Li, Z. et al. Comprehensive parameter space mapping of cell cycle dynamics under network perturbations. *ACS Synth. Biol.* **13**, 804–815 (2024).
24. Yang, Q. & Ferrell Jr, J. E. The Cdk1–APC/C cell cycle oscillator circuit functions as a time-delayed, ultrasensitive switch. *Nat. Cell Biol.* **15**, 519–525 (2013).
25. Rombouts, J. & Gelens, L. Synchronizing an oscillatory medium: the speed of pacemaker-generated waves. *Phys. Rev. Res.* **2**, 043038 (2020).
26. Rombouts, J. & Gelens, L. Analytical approximations for the speed of pacemaker-generated waves. *Phys. Rev. E* **104**, 014220 (2021).
27. Nolet, F. E. & Gelens, L. Mitotic waves in an import-diffusion model with multiple nuclei in a shared cytoplasm. *Biosystems* **208**, 104478 (2021).
28. Piñeros, L. et al. The nuclear-cytoplasmic ratio controls the cell cycle period in compartmentalized frog egg extract. *bioRxiv* https://doi.org/10.1101/2024.07.28.605512 (2024).
29. Hara, Y. & Merten, C. A. Dynein-based accumulation of membranes regulates nuclear expansion in *Xenopus laevis* egg extracts. *Dev. Cell* **33**, 562–575 (2015).
30. Cheng, X. & Ferrell Jr, J. E. Apoptosis propagates through the cytoplasm as trigger waves. *Science* **361**, 607–612 (2018).
31. Masui, Y. & Markert, C. L. Cytoplasmic control of nuclear behavior during meiotic maturation of frog oocytes. *J. Exp. Zool.* **177**, 129–145 (1971).
32. Murray, A. W. Cell cycle extracts. *Methods Cell Biol.* **36**, 581–605 (1991).
33. Schmidt, A., Rauh, N. R., Nigg, E. A. & Mayer, T. U. Cytostatic factor: an activity that puts the cell cycle on hold. *J. Cell Sci.* **119**, 1213–1218 (2006).
34. Yamamoto, T. M., Iwabuchi, M., Ohsumi, K. & Kishimoto, T. APC/C–Cdc20-mediated degradation of cyclin B participates in CSF arrest in unfertilized *Xenopus* eggs. *Dev. Biol.* **279**, 345–355 (2005).
35. Good, M. C. & Heald, R. Preparation of cellular extracts from *Xenopus* eggs and embryos. *Cold Spring Harb Protoc.* **2018**, https://doi.org/10.1101/pdb.prot097055 (2018).
36. Takagi, J. & Shimamoto, Y. High-quality frozen extracts of *Xenopus laevis* eggs reveal size-dependent control of metaphase spindle micromechanics. *Mol. Biol. Cell* **28**, 2170–2177 (2017).
37. Deming, P. & Kornbluth, S. Study of apoptosis in vitro using the *Xenopus* egg extract reconstitution system. *Methods Mol. Biol.* **322**, 379–393 (2006).
38. Huang, J.-H., Chen, Y., Huang, W. Y., Tabatabaee, S. & Ferrell Jr, J. E. Robust trigger wave speed in *Xenopus* cytoplasmic extracts. *Nat. Commun.* **15**, 5782 (2024).
39. Tyson, J. J. & Keener, J. P. Singular perturbation theory of traveling waves in excitable media (a review). *Phys. D: Nonlinear Phenom.* **32**, 327–361 (1988).
40. Elphick, C., Hagberg, A., Malomed, B. & Meron, E. On the origin of traveling pulses in bistable systems. *Phys. Lett. A* **230**, 33–37 (1997).
41. Hagberg, A. & Meron, E. Pattern formation in non-gradient reaction-diffusion systems: the effects of front bifurcations. *Nonlinearity* **7**, 805 (1994).
42. Rinzel, J. & Terman, D. Propagation phenomena in a bistable reaction-diffusion system. *SIAM J. Appl. Math.* **42**, 1111–1137 (1982).

43. Bode, M. Front-bifurcations in reaction-diffusion systems with inhomogeneous parameter distributions. *Phys. D: Nonlinear Phenom.* **106**, 270–286 (1997).

44. Puls, O. & Yang, Q. The rise of ultrafast waves. *Dev. Cell* **47**, 532–534 (2018).

45. Wu, Z., Su, M., Tong, C., Wu, M. & Liu, J. Membrane shape-mediated wave propagation of cortical protein dynamics. *Nat. Commun.* **9**, 136 (2018).

46. Baldin, V. & Ducommun, B. Subcellular localisation of human wee1 kinase is regulated during the cell cycle. *J. Cell Sci.* **108**, 2425–2432 (1995).

47. Trunnell, N. B., Poon, A. C., Kim, S. Y. & Ferrell, J. E. Ultrasensitivity in the regulation of Cdc25C by Cdk1. *Mol. Cell* **41**, 263–274 (2011).

48. Jin, M., Tavella, F., Wang, S. & Yang, Q. In vitro cell cycle oscillations exhibit a robust and hysteretic response to changes in cytoplasmic density. *Proc. Natl Acad. Sci.* **119**, e2109547119 (2022).

49. Edelstein, A., Amodaj, N., Hoover, K., Vale, R. & Stuurman, N. Computer control of microscopes using µManager. *Curr. Protoc. Mol. Biol.* **92**, 14.20.1–14.20.17 (2010).

50. Preibisch, S., Saalfeld, S. & Tomancak, P. Globally optimal stitching of tiled 3D microscopic image acquisitions. *Bioinformatics* **25**, 1463–1465 (2009).

51. Montagne, R., Hernández-García, E., Amengual, A. & San Miguel, M. Wound-up phase turbulence in the complex Ginzburg-Landau equation. *Phys. Rev. E* **56**, 151 (1997).

52. Gillespie, D. T. Exact stochastic simulation of coupled chemical reactions. *J. Phys. Chem.* **81**, 2340–2361 (1977).

53. Rackauckas, C. & Nie, Q. Differential equations.jl—a performant and feature-rich ecosystem for solving differential equations in Julia. *J. Open Res. Softw.* **5**, 15 (2017).

54. Puls, O. et al. Spatial heterogeneity accelerates phase-to-trigger wave transitions in frog egg extracts. https://doi.org/10.5281/zenodo.10583185 (2024).

Acknowledgements

Author contributions

O.P. and Q.Y. conceived and initiated the project. O.P., D.R.-R., L.G., and Q.Y. conceptualized the study. O.P. conducted the majority of the experiments, helped by M.J. D.R.-R. developed the data analysis codes, and analyzed the data together with O.P., F.T., and Y.K. D.R.-R. and Y.K. performed the deterministic and stochastic simulations, respectively. O.P., D.R.-R., Y.K., L.G., and Q.Y. wrote the manuscript. L.G. and Q.Y. supervised the study. All authors edited and approved the manuscript.

Competing interests

The authors declare no competing interests.

Additional information

Supplementary information The online version contains supplementary material available at https://doi.org/10.1038/s41467-024-54752-7.

Correspondence and requests for materials should be addressed to Lendert Gelens or Qiong Yang.

Peer review information Nature Communications thanks the anonymous reviewers for their contribution to the peer review of this work. A peer review file is available.

Reprints and permissions information is available at http://www.nature.com/reprints

Publisher's note Springer Nature remains neutral with regard to jurisdictional claims in published maps and institutional affiliations.